

Rotation of gap nodes in the topological superconductor

$\text{Cu}_x(\text{PbSe})_5(\text{Bi}_2\text{Se}_3)_6$

Mahasweta Bagchi,¹ Jens Brede,^{1,*} Aline Ramires,^{2,†} and Yoichi Ando^{1,‡}

¹*Physics Institute II, University of Cologne, D-50937 Köln, Germany*

²*Paul Scherrer Institute, CH-5232 Villigen PSI, Switzerland*

(Dated: July 18, 2023)

Abstract

Among the family of odd-parity topological superconductors derived from Bi_2Se_3 , $\text{Cu}_x(\text{PbSe})_5(\text{Bi}_2\text{Se}_3)_6$ (CPSBS) has been elucidated to have gap nodes. Although the nodal gap structure has been established by specific-heat and thermal-conductivity measurements, there has been no direct observation of the superconducting gap of CPSBS using scanning tunnelling spectroscopy (STS). Here we report the first STS experiments on CPSBS down to 0.35 K, which found that the vortices generated by out-of-plane magnetic fields have an elliptical shape, reflecting the anisotropic gap structure. The orientation of the gap minima is found to be aligned with the bulk direction when the surface lattice image shows twofold symmetry, but, surprisingly, it is rotated by 30° when twofold symmetry is absent. In addition, the superconducting gap spectra in zero magnetic field suggest that the gap nodes are most likely lifted. We argue that only an emergent symmetry at the surface, allowing for a linear superposition of gap functions with different symmetries in the bulk, can lead to the rotation of the gap nodes. The absence of inversion symmetry at the surface additionally lifts the nodes. This result establishes the subtle but crucial role of crystalline symmetry in topological superconductivity.

* brede@ph2.uni-koeln.de

† aline.ramires@psi.ch

‡ ando@ph2.uni-koeln.de

I. INTRODUCTION

Topological superconductivity is a current hot topic in condensed matter physics due to its close relevance to Majorana fermions [1]. However, not many materials have been conclusively identified as topological superconductors. The family of bulk superconductors derived from Bi_2Se_3 presents a rare case, in which odd-parity topological superconductivity has been well established [1, 2]. In this class of materials, despite the three-fold rotational symmetry of the lattice, bulk superconducting (SC) properties consistently show peculiar twofold symmetry [3–9] that points to the realization of an odd-parity gap function with E_u symmetry. Although this gap function is unconventional and strongly anisotropic, the superconductivity is nonetheless protected from disorder due to the generalized Anderson’s theorem, thanks to the additional orbital degrees of freedom and layered structure [10–12].

Interestingly, the E_u -symmetric gap function under D_{3d} symmetry is generally a linear superposition of two basis functions, conventionally called Δ_{4x} and Δ_{4y} , which have nodes along a mirror plane of the crystal lattice or normal to it, respectively. The coefficients of the superposition form the nematic director \mathbf{n} [13]. In the presence of a principal rotation axis with threefold symmetry, there are three degenerate superpositions of these basis functions, corresponding to three distinct nematic directors. The selection of one of these superpositions endows a nematic character to the SC state. Note that only the mirror-symmetry-protected nodes are expected to be robust under the D_{3d} symmetry, while others can be lifted by perturbations such as a warping term in the normal state electronic structure [13]. Elucidating the factors that dictate the nematic axis is important not only for understanding the topological superconductivity in the Bi_2Se_3 -based compounds but also for finding ways to manipulate the SC gap [14].

Experimentally, the orientation of the gap minima differs among experiments even for the same compound [2]. For example, in $\text{Cu}_x\text{Bi}_2\text{Se}_3$, the direction of the gap minima has been reported to be 90° rotated between bulk [4] and surface [15] measurements. In this regard, there is a complexity arising from the threefold rotational symmetry of the Bi_2Se_3 lattice, which allows for three equivalent rotational domains [2, 4]; when contributions from two or more domains are superposed, the apparent symmetry may look like, e.g., Δ_{4x} even when the true symmetry is Δ_{4y} [4, 16].

Fortunately, this complexity is absent in the superconductor $\text{Cu}_x(\text{PbSe})_5(\text{Bi}_2\text{Se}_3)_6$ (here-

after called CPSBS) [9, 11, 17] which has a monoclinic crystal structure and a topologically nontrivial twofold symmetric gap function [1, 18, 19]. Specifically, Andersen *et al.* [9] showed that the gap function in CPSBS has nodes located on the unique crystallographic mirror plane, giving rise to nodal superconductivity in the bulk, which was evinced by specific-heat [9] and thermal-conductivity [11] measurements in the mK-regime. In this work, we use scanning tunneling microscopy (STM) and spectroscopy (STS) to directly access the SC gap on the surface of CPSBS. On a relatively clean surface, we found that vortices generated under out-of-plane magnetic fields are elongated in a twofold-symmetric manner, and the elongation occurs in the direction perpendicular to the bulk gap nodes. This is contrary to the naive expectation that the coherence length should be longer along the direction of the gap nodes [15], but it is actually consistent with recent theoretical calculations which showed that the vortex anisotropy in a p -wave superconductor should rotate by 90° as a result of impurity scattering [20]. On a more disordered surface where the twofold lattice symmetry is smeared, we found that the vortex anisotropy axis is rotated by 30° , pointing to the rotation of the gap nodes/minima on the surface. Our symmetry analysis shows that rotation of the gap nodes is indeed possible in the presence of an emergent symmetry at the surface and, furthermore, the inversion symmetry breaking at the surface would lead to lifting of the nodes. The latter conclusion is consistent with the observed gap spectra. Our work hence offers a framework to understand the intricate relation between crystal symmetry and the gap function in a topological superconductor.

II. RESULTS

A. Elongated vortices

We examine the SC gap structure on the surface of CPSBS by applying an out-of-plane magnetic field and imaging the vortex lattice of CPSBS in the mixed state. Even though a major portion of the cleaved surface of CPSBS does not show superconductivity, we were able to observe superconductivity on the sample surface at roughly 17% of the total scan area (see [21] for details), which is slightly better than the case of $\text{Cu}_x\text{Bi}_2\text{Se}_3$ [15]. Figure 1(a,b) and (c,d) shows the spatially resolved normalized zero-bias conductance (ZBC) on the superconducting surface of CPSBS for two different samples, S-I and S-II, and for

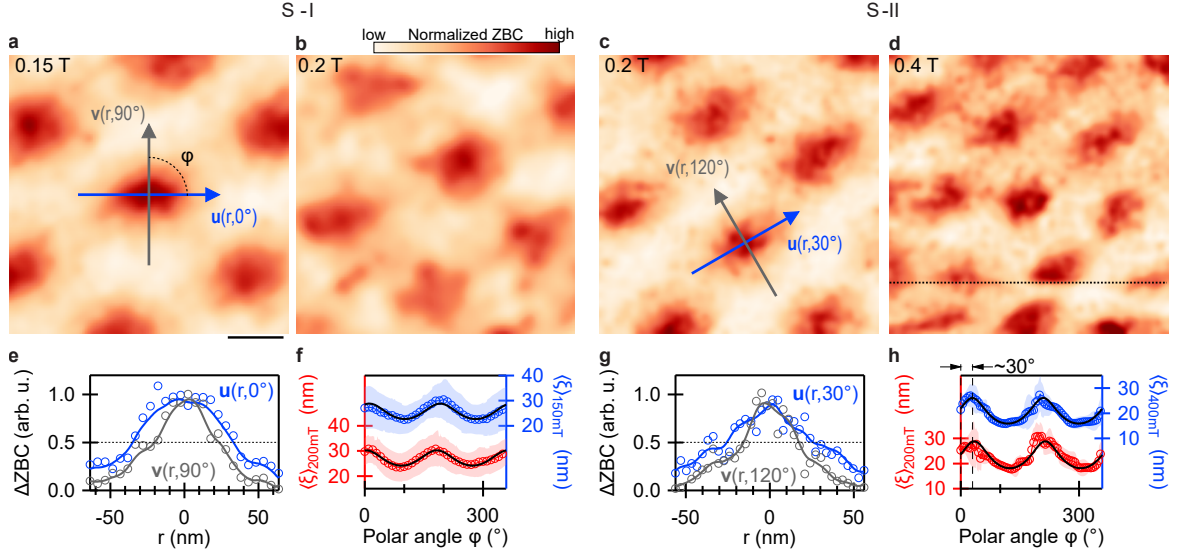


FIG. 1. **Elongated vortices in CPSBS.** (a,b) Normalized zero-bias conductance (ZBC) maps taken on sample S-I (a,b) in the out-of-plane magnetic field of 0.15 and 0.2 T. Stabilization parameters: $U = 5$ mV, $I = 200$ pA and $U_{\text{mod}} = 100 \mu\text{V}_p$. (c,d) Similar maps for sample S-II in 0.2 T and 0.4 T. Stabilization parameters: $U = 1$ mV, $I = 50$ pA and $U_{\text{mod}} = 100 \mu\text{V}_p$. Gaussian smoothing was applied to all maps to filter spatial variations of the ZBC smaller than the vortex size (unsmoothed data is shown in [21]). The discontinuity [dotted line in (d)] is due to the vortex lattice motion during the measurement. (e,g) Line profiles of the change in normalized ZBC (ΔZBC) taken across a vortex centre along the vectors shown in (a) and (c); solid lines and open circles are smoothed and raw data, respectively. (f,h) Angular dependence of the average vortex radius (ξ). Open circles denote the average of 53 (56) vortices measured for sample S-I at 0.15 T (0.2 T); for sample S-II, the average was from 6 (7) vortices at 0.2 T (0.4 T). The shaded area indicates the standard deviation and the solid black line is a fit to the ellipse equation. The polar angle was measured from the horizontal axis, which is parallel to the monoclinic b -axis.

out-of-plane magnetic fields between 0.15 and 0.4 T (additional data for other fields are shown in [21]). A vortex lattice is clearly resolved, and the vortex density increases with increasing field. Importantly, all the observed vortices are deformed — the vortices in sample S-I are roughly elongated along the horizontal axis, while those in sample S-II are rotated by about 30° in comparison.

Naively, one would expect that elongated vortices reflect an anisotropy in the Ginzburg-Landau (GL) in-plane coherence length, which results from the SC gap anisotropy in k -space, with the longest (shortest) coherence length associated with directions for which the gap value is the smallest (largest) [15]. However, it was recently pointed by theory that the local density of states (LDOS) around vortices imaged by STM experiments can acquire

different geometries depending on the strength of impurity scattering [20]. In particular, it was shown that for a p -wave superconductor, the LDOS is elongated along the the direction perpendicular to the gap nodes, in contrast to the naive GL prediction for clean systems. We will discuss the relation between the vortex elongation and the gap nodes/minima in Sec. II-C.

It is prudent to mention that a vortex-shape anisotropy can also be caused by a Fermi-velocity anisotropy [22, 23]. However, the ARPES measurements on superconducting CPSBS [24] found no such anisotropy within the experimental error of $\sim 2\%$. Even if there were some unexpected Fermi-velocity anisotropy in the region of the vortex lattice, we do not expect it can lead to an anisotropy of the vortex shape in the present case, because CPSBS is in the dirty limit [21] and a vortex-shape anisotropy cannot result purely from a Fermi-velocity anisotropy in the dirty limit [22]. Also, a vortex can appear elongated if the magnetic field is not perpendicular to the sample surface [25]; to dismiss this possibility, we intentionally tilted the applied magnetic field by about 10° both along the short and long vortex axes (see Fig. S9 in [21]) and observed no significant change in the anisotropy. Hence, it can be concluded that the elongation of the vortex stems from the anisotropic gap.

To quantify the vortex elongation, we first determine the vortex lattice (see [21] for details) and then take line-cuts of the ZBC at each lattice site corresponding to a vortex centre. Examples of such line-cuts are shown in Fig. 1 (e) and (g) for directions crossing the vortex shown in (a) and (c), respectively. We follow Sera *et al.* [20] to define the vortex-core radius ξ as the half width at half maximum, and determined it as a function of the polar angle φ . We obtained this $\xi(\varphi)$ for 53 (56) vortices in sample S-I at 0.15 T (0.2 T) and for 6 (7) vortices in sample S-II at 0.2 T (0.4 T). Note that ξ is not necessarily equal to the GL coherence length due to the scattering-induced LDOS [20]. The $\xi(\varphi)$ data are averaged over all vortices in each data set to yield $\langle \xi(\varphi) \rangle$, which is plotted for sample S-I in Fig. 1 (f) and for sample S-II in (h). The observed φ -dependence is reasonably well fit by the ellipse equation, and the fitting gives the ratio between the major and minor axes, $\gamma \equiv \langle \xi_{\text{major}} \rangle / \langle \xi_{\text{minor}} \rangle$, of ~ 1.25 (~ 1.55) for sample S-I (S-II). The fitting also gives the rotation angle of $\sim 30^\circ$ for the vortices in sample S-II.

B. Superconducting gap spectra

As discussed above, our observation of elongated vortices points to an anisotropic SC gap. To investigate the anisotropy in the SC gap function, we analyzed the representative dI/dU -spectra (Fig. 2) measured in zero field at the lowest fridge temperature of 0.35 K for samples S-I and S-II. We fit the spectra by using a generalization of Dynes formula [26] for the momentum-resolved superconducting DOS,

$$N_{\mathbf{k}}(E) = \left| \text{Re} \left[(E - i\Gamma) / \sqrt{(E - i\Gamma)^2 - \Delta_{\mathbf{k}}^2} \right] \right|, \quad (1)$$

where we assume a circular Fermi surface. Γ is an effective broadening parameter due to pair-breaking scattering and $\Delta_{\mathbf{k}}$ is the SC gap that can have a \mathbf{k} -dependence. We fit a twofold symmetric gap with $\Delta_{\mathbf{k}} = \Delta_0 + \Delta_1 |\cos \theta_{\mathbf{k}}|$: when the gap is nodal, $\Delta_0 = 0$. The

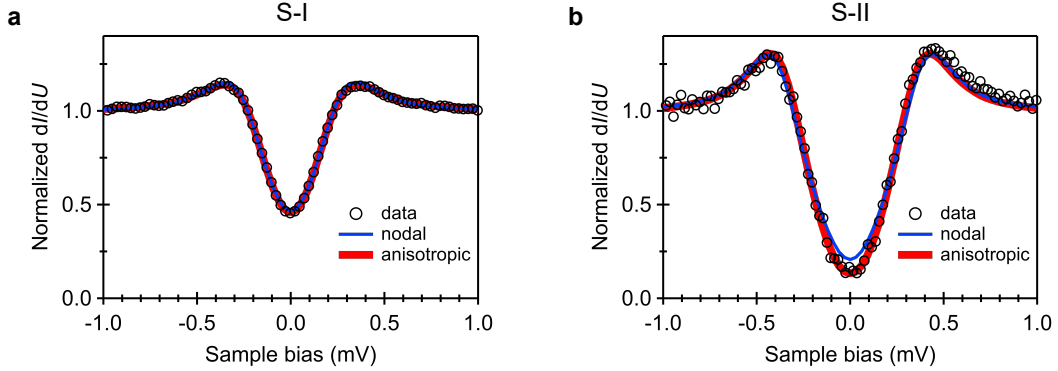


FIG. 2. Superconducting gap spectra. Representative high-resolution gap spectra taken in zero field, at the base temperature of 0.35 K and in the same area as the vortex maps. The spectrum in (a) is a result of averaging 10000 individual spectra covering an area of $(500 \text{ nm})^2$, while the data in (b) is after averaging 5000 individual spectra taken at the same spot to enhance the resolution. The fits of the data to Eq. (1) assuming two different gap functions [nodal (blue) and node-lifted anisotropic (red) types] are overlayed on the data. In these fits, the effective temperature was fixed at 0.7 K. The set of parameters $(\Delta_0, \Delta_1, \Gamma)$ obtained from the fits in (a) for sample S-I are $(0, 0.26, 0.03)$ and $(0.07, 0.18, 0.05)$ for the nodal and node-lifted scenarios, respectively, and those for sample S-II in (b) are $(0, 0.39, 0)$ and $(0.11, 0.26, 0.01)$ for the two scenarios (all in mV unit). Any error of the fitting routine is well below the experimental uncertainty due to the spatial inhomogeneity of the total gap magnitude, which was about 0.05 meV in each area [21]. Stabilization parameters: $U = 5 \text{ mV}$, $I = 500 \text{ pA}$ for sample S-I (a) and $U = 3 \text{ mV}$, $I = 50 \text{ pA}$ for sample S-II (b).

tunnelling conductance dI/dU is given by

$$\frac{dI}{dU} \propto \int N_{\mathbf{k}}(E) f'(E + eU) d\mathbf{k} dE, \quad (2)$$

where $f(E)$ is the Fermi-Dirac distribution function at the effective temperature T_{eff} . The effective temperature of our STM experiments at the fridge temperature of 0.35 K was independently determined by a measurement of pure Nb [27] to be 0.7 K, so we fixed $T_{\text{eff}} = 0.7$ K and used Γ , Δ_0 and Δ_1 as fitting parameters.

In Fig. 2, we show fits to two different types of gap function: (i) nodal gap ($\Delta_0 = 0$) and (ii) twofold symmetric gap with lifted nodes ($\Delta_0 \neq 0$). As is described in detail in [21], the size of the SC gap on the CPSBS surface varies with location. Thanks to a relatively large local gap, the data in Fig. 2(b) from sample S-II have a low ZBC which helps to infer if the nodes are lifted: The nodal fit of the spectrum yields a ZBC that is higher than the data even for $\Gamma = 0$, which is clearly unreasonable given the dirty-limit nature of CPSBS [21]. On the other hand, a reasonable fit is obtained for the anisotropic gap with lifted nodes, yielding $\Delta_0 = 0.11$ meV and $\Delta_1 = 0.26$ meV with $\Gamma = 10$ μ eV. Hence, the data in Fig. 2(b) strongly suggest that the nodes are lifted at the surface. Here we should note that the conclusion of lifted nodes is based on the fits to the commonly-assumed sinusoidal gap function, and it may not be valid if the anisotropic gap has a non-sinusoidal function with unusually steep node. The large anisotropy ratio $(\Delta_0 + \Delta_1)/\Delta_0 \simeq 3.4$ implies a pronounced minima in the gap function, which is consistent with the finite quasiparticle scattering even in the absence of vortices. Due to a smaller local gap resulting in a large ZBC, the data in Fig. 2(a) from sample S-I do not allow us to distinguish between nodal and the node-lifted scenarios; nevertheless, the fit with the anisotropic gap function yields a reasonable result with an anisotropy ratio of ~ 3.6 . In fact, the spectra obtained at all the SC regions are consistent with the anisotropic gap function (see Fig. S11 in [21]), even though the value of Δ_0 and Δ_1 varies significantly. This large variation appears to reflect the fact the the superconductivity in CPSBS (and in all other Bi_2Se_3 -based superconductors) is weakened or disappear at a larger part of the surface, whose origin is a topic of on-going research: For example, in a recent paper [27] it was proposed that a strong electric field due to intrinsic surface band bending may break Cooper pairs near the surface. In the case of CPSBS, the strength of surface band bending would vary depending on the density of Cu dopants found

on the surface.

To strengthen the conclusion of the anisotropic gap, we performed additional experiments on sample S-III to measure the dependence of the SC gap spectra on the direction of the in-plane magnetic field, φ (see [21] for details). The φ -dependence of the spectra, in particular the conductance at zero bias, is clearly twofold symmetric (see Fig. S12 in [21]). A similar phenomenon was reported for $\text{Cu}_x\text{Bi}_2\text{Se}_3$ [15] and was taken as additional evidence for an anisotropic gap. These observations are also in good agreement with the theoretical prediction by Nagai [28], who showed that the angular dependence of the zero-energy density of states has deep minima when the in-plane magnetic field is aligned with the direction of the nodes in the Δ_4 gap realized in $\text{Cu}_x\text{Bi}_2\text{Se}_3$.

C. Orientation of the gap minima

We now turn to the topographic images of CPSBS and those of pristine $(\text{PbSe})_5(\text{Bi}_2\text{Se}_3)_6$ (called PSBS) to identify the orientation of the gap minima. Figure 3(a) shows the schematics of the crystal structure of PSBS/CPSBS. Upon cleaving the PSBS crystal, one usually obtains a surface that is terminated by a single quintuple layer (QL) of the Bi_2Se_3 unit on top of the PbSe layer [29]. Figure 3(d) shows a typical topograph on such a surface, where a clear one-dimensional (1D) stripe pattern with atomically resolved top Se layer is observed. Although the lattice in CPSBS is more disordered due to Cu intercalation, a similar stripe pattern is observed in atomic-resolution images on a SC area of CPSBS of sample S-I [Fig. 3(f)] as well as on a non-superconducting (NSC) area of sample S-II [Fig. 3(e)]. The stripe corrugation is less pronounced in the SC area of sample S-I [Fig. 1(g)].

The 1D stripe can be understood as a commensuration effect (similar to a moiré pattern) arising from the stacking of the square PbSe lattice and the hexagonal Bi_2Se_3 lattice. One can see in Fig. 3(a) that the crystal structure repeats every six Se atoms in the layer 5 and every five Pb atoms in layer 6 along the a -axis, and this repetition defines the unit length along the a -axis. As shown in Fig. 3(c), the stripe periodicity agrees with the length of the monoclinic a -axis, which clearly indicates that the stripes come from this commensuration of Se and Pb sublattices. This in turn allows for a unique determination of the in-plane monoclinic lattice vectors on the hexagonal top Se layer, i.e., the stripes are running along the b -axis. While we were not able to resolve the crystal lattice in the SC area of sample S-II

where the vortex lattice shown in Fig. 1(c,d) was recorded (a similar case was reported by Tao *et al.* [15] for $\text{Cu}_x\text{Bi}_2\text{Se}_3$), we know from X-ray diffraction analysis that in our CPSBS sample the orientation of the monoclinic axes is macroscopically identical. This is further verified in STM since we only observed one fixed orientation of the 1D-stripe with respect to our scan coordinates, globally.

In Fig. 3(b), we replot the anisotropic ξ with respect to the hexagonal lattice and the monoclinic axes for both samples S-I and S-II. Focusing first on the data for S-I, it is to

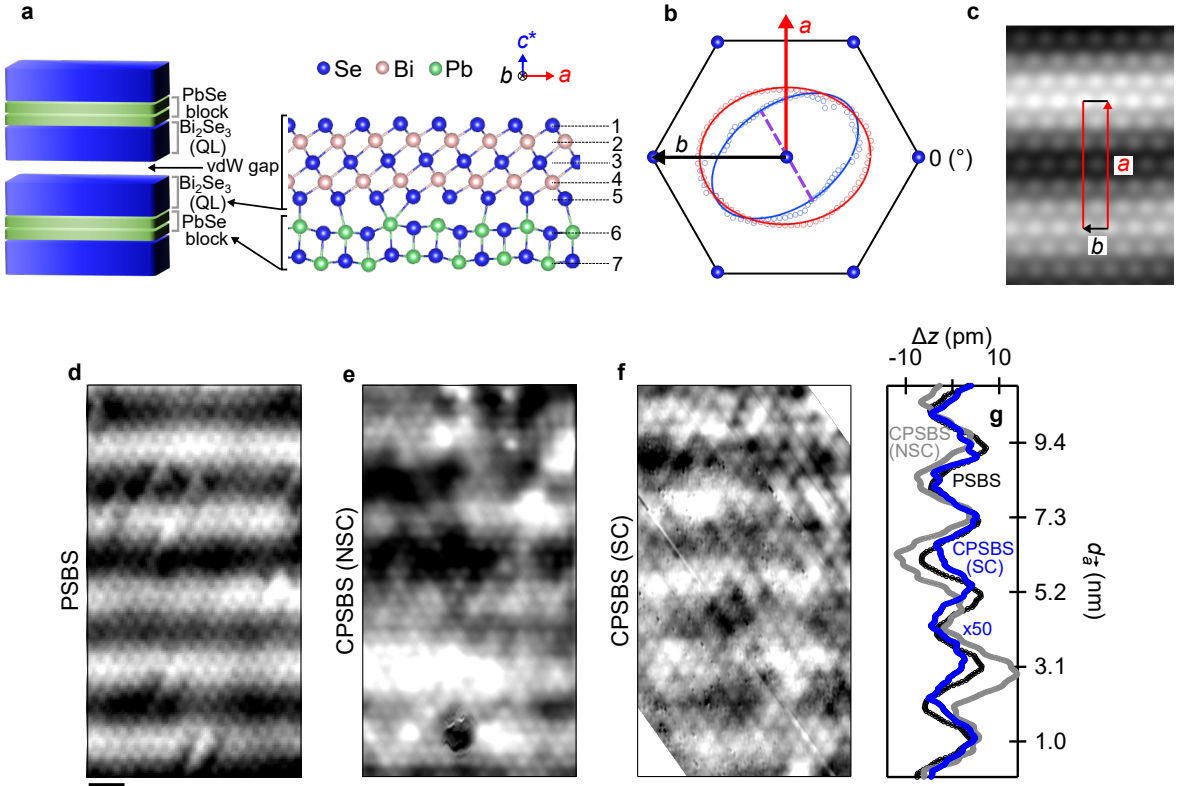


FIG. 3. Crystal structure and the gap anisotropy. (a) Schematics of the crystal structure of PSBS. (b) Average profile (open circles) and the fit to the ellipse equation (solid line) of vortices at 0.2 T for sample S-I (red) and S-II (blue) [the same data as in Figs. 1(f) and (h)] with respect to the top Se lattice and the monoclinic a and b axes; the mirror plane is parallel to a . (c) Fourier-filtered image of (d) overlaid with the monoclinic unit vectors; the stripe periodicity of ~ 2.1 nm agrees with the a unit length. (d) Atomically resolved topmost Se layer on the cleaved surface of PSBS showing 1D stripes running across the whole surface. The stripe pattern is also observed on the non-superconducting areas of the CPSBS surface in sample S-II (e) and the superconducting area of sample S-I (f). Scale bar corresponds to 1 nm. (g) Averaged STM height profile along the vertical direction in (d) to (f). Scan parameters: $U = 900$ mV, $I = 20$ nA for (d); $U = 30$ mV, $I = 500$ pA for (e); $U = 900$ mV, $I = 200$ pA for (f).

be remarked that the vortex core is elongated roughly along the monoclinic b -axis, whereas the gap nodes in the bulk lie along the a -axis [9]. This fact indicates that the vortex-shape anisotropy is not dictated by the GL coherence length anisotropy but by the maxima of the LDOS in the presence of impurity scattering. A recent theoretical work has reported that the maxima in the LDOS can be rotated by 90° in the presence of impurity scattering [20]. This result can be understood in terms of the quasiparticle trajectory picture, which has been useful for understanding the rotation of vortices as a function of applied bias [30–32]. The effect of impurities in superconductors can be understood in terms of a self-energy renormalization of the frequency and gap matrices [33] introduced by a scattering potential. For an anisotropic s -wave superconductor, impurities self-average the gap to become isotropic, so any anisotropy in the LDOS promoted by the anisotropy of the gap is lost in the dirty limit. In contrast, in sign-changing nodal superconductors, impurities lead to a renormalization of the frequency, but not of the superconducting gap, as it averages to zero [33]. This renormalization can be understood as an effective bias, as it increases the frequency, and the conclusions for the rotation of the vortex anisotropy as a function of bias can then be generalized to the rotation of the vortex anisotropy as a function of impurity scattering. Figure 4 gives a schematic representation of this mechanism.

It is worthwhile to note that p -wave superconductivity is commonly known to be fragile against impurity scattering; however, in CPSBS the generalized Anderson theorem [11] protects the unconventional pairing even in the dirty limit. Note also that this impurity effect on the vortex shape was not considered in the previous work on $\text{Cu}_x\text{Bi}_2\text{Se}_3$ [15], which concluded that the gap minima at the surface are 90° rotated compared to the bulk.

Interestingly, the elongation axis of the vortices in sample S-II shown in Fig. 1(c,d) is 30° rotated from that in sample S-I. Following the conclusion that the vortex elongation occurs in the direction of gap maxima in CPSBS, the data in Fig. 1(c,d) suggest that on the SC surface of sample S-II, the gap minima are rotated from the monoclinic a axis by 30° , which is perpendicular to one of the mirror planes of D_{3d} symmetry and corresponds to the Δ_{4y} gap. In correspondence with this result, the in-plane magnetic-field-direction dependence of the gap spectra observed in sample S-III, which was discussed in Sec. II-B, also shows that the gap minima is rotated from the a axis by $\sim 20^\circ$ (see [21] for details). As shown in Fig. S13 in [21], the SC areas of both samples S-II and S-III are so disordered that the stripe pattern indicating the twofold symmetry of the lattice is no longer observed. This implies

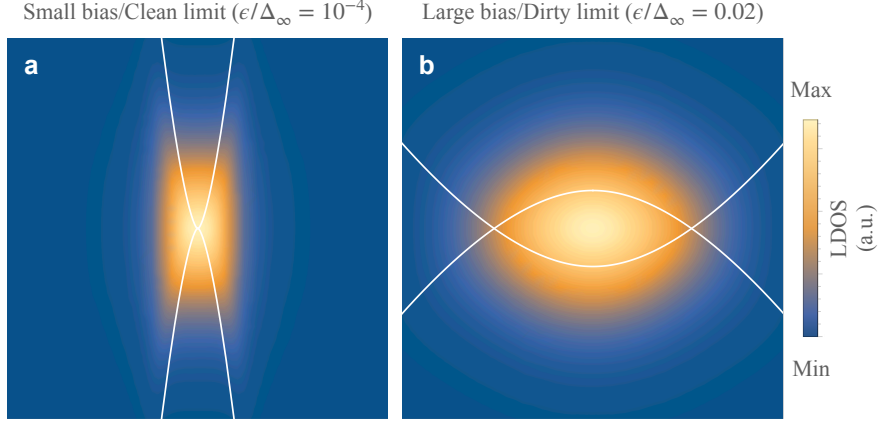


FIG. 4. **Quasiclassical trajectory picture.** (a) Small bias or clean limit, with small ϵ/Δ_∞ ratio. (b) Large bias or dirty limit with larger ϵ/Δ_∞ ratio. The enveloping curves of the quasiparticle paths at which the LDOS diverges are shown in white lines. The plots follow the analytical form given by Nagai *et al.* [31] [Eq. (3.45) of their paper] for a nodal superconductor with two-fold symmetry, $\lambda(\theta) = \cos(\theta)$. The density plots correspond to the LDOS given by the integral over the poles determined by the enveloping curves smeared by $\delta/\Delta_\infty = 0.05$ and with an isotropic exponential decay characterized by $l/\xi_0 = 400$. Here Δ_∞ is the gap magnitude in the bulk, ϵ is the energy scale of either the bias or the scattering rate, and ξ_0 the coherence length. The field of view corresponds to $0.2\xi_0$ along the x and y directions.

that the threefold symmetry of the Bi_2Se_3 QLs is effectively restored due to disorder in both samples. In the next section, we argue that the rotation of the gap minima observed on the SC surface of samples S-II and S-III can be understood as a consequence of this emergent symmetry.

III. THEORETICAL ANALYSIS

We now present a symmetry analysis which provides a consistent picture for the above observations, under the assumption that the superconductivity observed on the surface inherits the unconventional pairing from the bulk. We emphasize that, although the nature of the superconductivity on the surface is apparently different from that of the bulk, it must be unconventional itself, because vortices cannot be anisotropic in the dirty limit of a conventional superconductor.

We start the discussion from the perspective of the Bi_2Se_3 QLs with D_{3d} point group symmetry. The minimal model for the normal state electronic structure that properly captures the topological properties of the bands is given in terms of two effective orbitals with

opposite parity formed by a symmetric, labelled as 1, or antisymmetric, 2, combination of p_z orbitals within the QLs [34, 35]. In the orbital-spin basis $\Phi_{\mathbf{k}}^\dagger = (c_{1\uparrow}^\dagger, c_{1\downarrow}^\dagger, c_{2\uparrow}^\dagger, c_{2\downarrow}^\dagger)_{\mathbf{k}}$, the normal-state Hamiltonian can be parametrized as:

$$\hat{H}_0(\mathbf{k}) = \sum_{a,b} h_{ab}(\mathbf{k}) \hat{\tau}_a \otimes \hat{\sigma}_b, \quad (3)$$

where $\hat{\tau}_{a=1,2,3}$ are Pauli matrices encoding the orbital degrees of freedom (DOF), $\hat{\sigma}_{b=1,2,3}$ are Pauli matrices encoding the spin DOF, and $\hat{\tau}_0$ and $\hat{\sigma}_0$ are two-dimensional identity matrices in orbital and spin space, respectively. In the presence of time-reversal [acting as $\hat{\Theta} = K\hat{\tau}_0 \otimes (i\hat{\sigma}_2)$, where K stands for complex conjugation] and inversion (implemented as $\hat{P} = \hat{\tau}_3 \otimes \hat{\sigma}_0$) symmetries, the only allowed terms in the Hamiltonian have indexes $(a, b) = \{(0, 0), (2, 0), (3, 0), (1, 1), (1, 2), (1, 3)\}$. The properties of the $\hat{\tau}_a \otimes \hat{\sigma}_b$ matrices under the point group operations allow us to associate each of these terms to a given irreducible representation (irrep) of D_{3d} , therefore constraining the momentum dependence of the form factors $h_{ab}(\mathbf{k})$ by symmetry. More details on the description of the normal state are given in [21]. The important features to keep in mind are the following: (0, 0) and (3, 0) correspond to intra-orbital hopping, (2, 0) corresponds to inter-orbital hopping, (1, a), with $a = \{1, 2, 3\}$ correspond to spin-orbit coupling terms. In particular, (1, 3) is associated with trigonal warping and is very small within the parameter range of validity of this effective model [35].

Following the parametrization of the normal state, the order parameters can be generally written as:

$$\hat{\Delta}(\mathbf{k}) = \sum_{a,b} d_{ab}(\mathbf{k}) \hat{\tau}_a \otimes \hat{\sigma}_b (i\hat{\sigma}_2). \quad (4)$$

Focusing on local pairing mechanisms, the allowed momentum-independent gap matrices are associated with antisymmetric matrices $\hat{\tau}_a \otimes \hat{\sigma}_b (i\hat{\sigma}_2)$. These can be classified according to the irreps of the of D_{3d} point group, as displayed in the second column of Table I [18].

The QLs of Bi_2Se_3 have D_{3d} symmetry. In CPSBS, the presence of the PbSe layers reduces the point group symmetry from D_{3d} to D_{1d} , and the irreps are mapped according to the third column of Table I. The SC order parameter in the bulk of CPSBS is believed to be of the form [2, 2], given its twofold symmetry and the presence of nodes along the mirror plane [9, 11]. This is an odd-parity order parameter which is inter-orbital and spin-triplet in

$[a,b]$	D_{3d}	D_{1d}	C_{1v}	C_{3v}
$[0,0]$	A_{1g}	A_{1g}	A_1	A_1
$[3,0]$				
$[2,3]$	A_{1u}	A_{1u}	A_2	A_2
$[1,0]$	A_{2u}	A_{2u}	A_1	A_1
$[2,1]$	E_u	A_{2u}	A_1	E
$[2,2]$		A_{1u}	A_2	

TABLE I. **Classification of superconducting order parameters.** Here we focus on momentum-independent SC order parameters in the microscopic basis for materials in the family of Bi_2Se_3 . The $[a, b]$ indexes in the first column correspond to the parametrization of the SC gap function according to Eq. 4. The second to fifth columns give the irreducible representation associated with each order parameter for the cases of D_{3d} , D_{1d} , C_{1v} , and C_{3v} point group symmetry, respectively.

nature. Note that, in the case of D_{1d} symmetry, this order parameter belongs to A_{1u} irrep. This is a one-dimensional irrep and the notion of nematicity does not apply as the threefold symmetry is explicitly broken by the lattice. Note, though, that the order parameter with indices $[2, 3]$ belongs to the same A_{1u} symmetry channel in D_{1d} . This means that an order parameter in A_{1u} is generally a linear superposition of $[2, 2]$ and $[2, 3]$. Even if pairing is primarily driven by interactions promoting the order parameter $[2, 2]$, the combination of spin-orbit coupling terms $(1, 2)$ and $(1, 3)$ in the normal state Hamiltonian could lead to the development of SC correlations with $[2, 3]$ character. Nevertheless, as the trigonal warping term $(1, 3)$ is small in the Bi_2Se_3 -family of compounds [35], the corresponding mixing should also be small in the bulk of CPSBS, leading to a lifting of nodes that might be too small to be observed experimentally. This information is schematically conveyed in the second row of Figure 5.

At the surface of CPSBS inversion symmetry is broken and the point group is reduced to C_{1v} . The irreps associated to the order parameters with momentum-independent gap matrices are mapped according to the fourth column of Table I. Now the order parameter $[2, 2]$ belongs to irrep A_2 , and any order parameter in this symmetry channel should again be a linear superposition of $[2, 2]$ and $[2, 3]$. Note that due to inversion symmetry breaking at the surface, the normal-state Hamiltonian includes all (a, b) coefficients, allowing for multiple pairs of terms in the normal state to promote the mixing of the $[2, 2]$ and $[2, 3]$ order parameters (see detailed discussion in [21]). These surface terms in the normal-state Hamiltonian contribute further to the lifting of gap nodes, as illustrated in the third row of

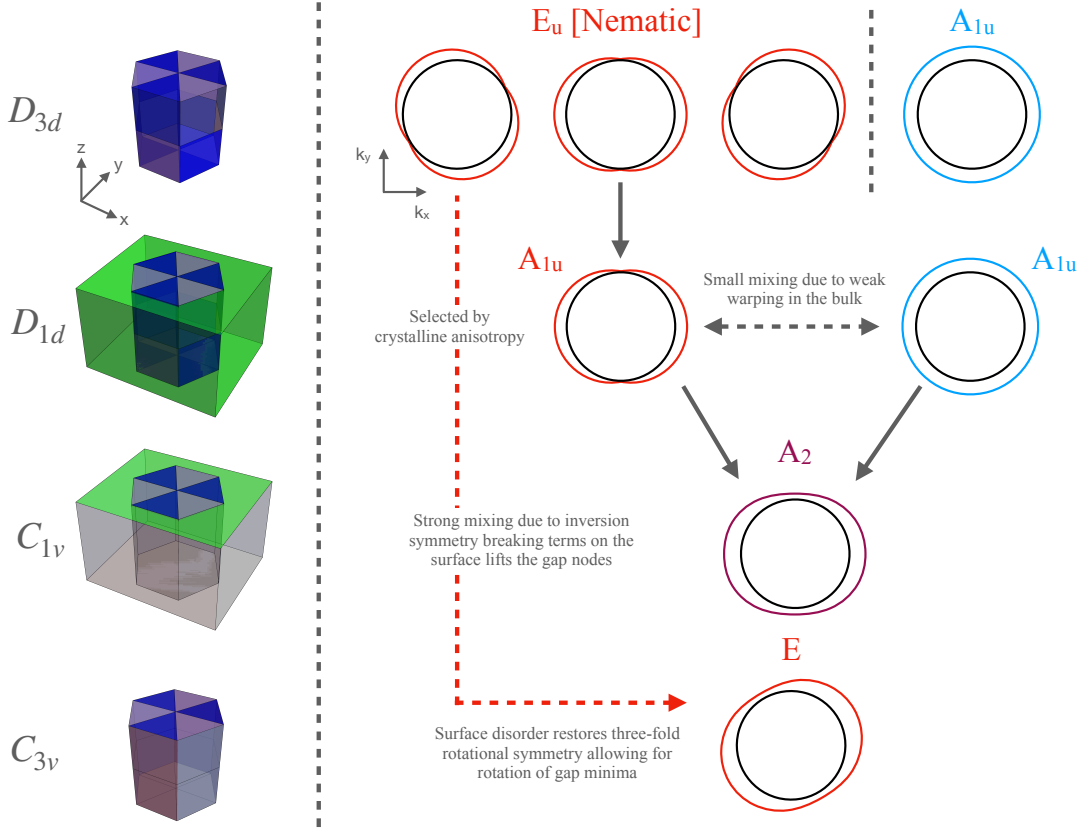


FIG. 5. **Symmetry analysis of the superconducting order parameter.** Left: Representative objects following the same point group symmetries as Bi_2Se_3 (D_{3d}), CPSBS (D_{1d}), and the surface of CPSBS (C_{1v} or C_{3v} , without or with disorder, respectively). The colour of the objects matches the corresponding Bi_2Se_3 and PbSe blocks in Figure 3(a). Right: SC gaps (coloured lines) at the Fermi surfaces (black circles) for the symmetry channels relevant for the discussion in the text. More details on the parameters used to generate the figures for each symmetry scenario are given in the Supplementary Information [21].

Figure 5, so that the node lifting at the surface would be stronger than that in the bulk. Here it should be emphasized that, as any gap in C_{1v} should still be symmetric or antisymmetric under reflections along the $k_y k_z$ -plane, the gap cannot be rotated under these symmetry considerations. For a rotation of gap nodes or gap minima to take place, a mixing of order parameters in different symmetry channels of C_{1v} would be required.

A possible origin of such a mixing is the strong disorder at the surface. The rotation of the gap minima was detected only in locations at which no stripe pattern could be observed by STM (see Fig. S13 in [21]), suggesting that in these disordered areas the effect of the PbSe layers is weakened and the threefold rotational symmetry present in the Bi_2Se_3 layers is

effectively restored. Under these considerations, the point group symmetry at the disordered surface can be identified as C_{3v} . Interestingly, this point group has a two-dimensional irrep labelled as E , which would allow for mixing of gaps $[2, 2]$ and $[2, 1]$ that are associated with different irreps in C_{1v} . Under the C_{3v} symmetry, by changing the mixing of these two order parameters in the absence of warping, we find that the gap minima can be tuned to any position along the circular Fermi surface. In particular, a ratio $d_{21}/d_{22} = 1$ generates minima at 30° from the bulk nodes. While the stability of this particular ratio requires an analysis of the energetics of the system, which is beyond the scope of this paper, the rotation by 30° corresponds to having the nodes along the a -axis of the hexagonal notation [9] for D_{3d} symmetry. It is plausible that this ratio is in fact stable, as this is the direction of the nodes realized in $\text{Cu}_x\text{Bi}_2\text{Se}_3$.

The last row of Figure 5 schematically shows a gap that could be generated at the surface under these considerations. Here, it should be remarked that the two-component nature of the order parameter in the quintuple layers of Bi_2Se_3 -based materials with D_{3d} symmetry is a necessary condition to explain the rotation of the gap at the surface of CPSBS. Therefore, the tunnelling spectra and the vortex anisotropy observed in our experiment provides one more piece of evidence for the intrinsically nematic nature of the SC gap in Bi_2Se_3 -based materials.

IV. DISCUSSIONS

We start our discussions by revisiting some of the experimental findings on $\text{Cu}_x\text{Bi}_2\text{Se}_3$ samples. Some of the discrepancies between the bulk [4] and the surface [15] regarding the direction of the gap minima may be resolved by considering the effect of impurity scattering discussed in Sec. II-C. However, in the literature, even in the bulk measurements on $\text{Cu}_x\text{Bi}_2\text{Se}_3$, there are reports which differ in the position of the gap minima with respect to the underlying lattice by 90° [3, 4]. Recent Knight-shift measurements [16] ruled out a multidomain effect in the bulk of the sample which was previously proposed [4] as the possible reason for the different orientations of the gap. It was proposed in [16] that the specific local environment in the sample caused by lattice distortion or strain from dopant intercalation and/or quenching (which is necessary for obtaining superconductivity) may be responsible for determining the nematic axis. A high-resolution x-ray diffraction (XRD)

experiment on $\text{Sr}_x\text{Bi}_2\text{Se}_3$ reported a tiny ($\sim 0.02\%$) in-plane lattice distortion [36], while a multimodal synchrotron XRD experiment with a slightly lower resolution did not find any distortion [37]. Therefore, the situation in doped- Bi_2Se_3 superconductors is complicated and it is still unclear what dictates the orientation of the gap minima in them.

In contrast, the orientation of the gap minima in the bulk of CPSBS is robust due to the reduced symmetry of the crystal lattice which has only one mirror plane, and the rotation of the gap minima observed here is a pronounced manifestation of the decisive role of crystalline symmetry in determining the anisotropic axis of the SC gap. The rotation of the gap minima also signifies the intrinsically nematic nature of the SC order parameter in Bi_2Se_3 -based materials, which suggests that the pairing mechanism must be the same for all superconductors in this family of materials.

It is useful to mention that according to the theoretical calculations reported in [20], the effect of impurity scattering is different for p -wave and anisotropic s -wave order parameters even when the angular dependence of the gap magnitude $|\Delta_{\mathbf{k}}|$ is the same; in the latter case, there is no sign change in the anisotropic SC gap and the vortex shape becomes isotropic in the presence of strong scattering. Therefore, the observation of elongated vortices in the dirty limit gives additional evidence for the topological odd-parity gap function.

The present result on CPSBS, taken together with the complications in the orientation of the gap minima in $\text{Cu}_x\text{Bi}_2\text{Se}_3$, clearly shows that the odd-parity gap function is highly sensitive to crystal symmetry in the topological superconductors derived from Bi_2Se_3 . The symmetry-based analysis of the possible superpositions of different gap functions presented here gives a useful framework to understand odd-parity topological superconductors.

Methods

Material: We grew $(\text{PbSe})_5(\text{Bi}_2\text{Se}_3)_6$ single crystals using a modified Bridgeman method as described previously [9, 17]. Cu was electrochemically intercalated using the recipe of Kriener *et al.* [38] with a nominal x value of 1.36. The SC shielding fraction of the resulting CPSBS sample was measured using a Quantum Design superconducting quantum interference device (SQUID) magnetometer (see Fig. S1 in [21]) and was 59% for sample S-I and 61% for sample S-II.

STM experiments: STM experiments were carried out under UHV conditions with a commercial system (Unisoku USM1300) operating at 0.35 K. STM images were recorded in

the constant-current mode at the set current I and sample bias voltage U . dI/dU curves and dI/dU maps were obtained either using a lock-in amplifier by modulating U_{bias} and demodulating I , or by recording a series of I - U curves followed by numerical differentiation. The dI/dU maps displayed in Fig. 1 were smoothed by using a standard Gaussian filter with the smallest (3×3 points) kernel, corresponding to $15 \times 15 \text{ nm}^2$ (a), $20 \times 20 \text{ nm}^2$ (b) and $9.35 \times 9.35 \text{ nm}^2$ (c,d), with up to three iterations. The dI/dU spectra displayed in Fig. 2 were obtained by taking the numerical derivative of raw I - U data and subsequently applying a simple low-pass filter (binominal 21 passes). All STM data were analyzed using Igor Pro 9. We used in-house electrochemically etched W tips, first prepared on the Cu(111) crystal. Tip forming is done until a clean signature of the surface state is observed in spectroscopy. Prior to STM measurements, the crystals were cleaved under UHV conditions as described in [27].

Acknowledgment: This project has received funding from the European Research Council (ERC) under the European Union’s Horizon 2020 research and innovation programme (grant agreement No 741121) and was also funded by the DFG under CRC 1238 - 277146847 (Subprojects A04 and B06) as well as under Germany’s Excellence Strategy - Cluster of Excellence Matter and Light for Quantum Computing (ML4Q) EXC 2004/1 - 390534769. AR is supported by the Swiss National Science Foundation through the Ambizione Grant No. 186043.

-
- [1] Sato, M. & Ando, Y. Topological superconductors: a review. Rep. Prog. Phys. **80**, 076501 (2017).
 - [2] Yonezawa, S. Nematic superconductivity in doped Bi_2Se_3 topological superconductors. Condens. Matter **4**, 2 (2019).
 - [3] Matano, K., Kriener, M., Segawa, K., Ando, Y. & Zheng, G.-q. Spin-rotation symmetry breaking in the superconducting state of $\text{Cu}_x\text{Bi}_2\text{Se}_3$. Nat. Phys. **12**, 852–854 (2016).
 - [4] Yonezawa, S. et al. Thermodynamic evidence for nematic superconductivity in $\text{Cu}_x\text{Bi}_2\text{Se}_3$. Nat. Phys. **13**, 123–126 (2017).
 - [5] Liu, Z. et al. Superconductivity with topological surface state in $\text{Sr}_x\text{Bi}_2\text{Se}_3$. J. Am. Chem. Soc. **137**, 10512–10515 (2015).

- [6] Pan, Y. et al. Rotational symmetry breaking in the topological superconductor $\text{Sr}_x\text{Bi}_2\text{Se}_3$ probed by upper-critical field experiments. Sci. Rep. **6**, 28632 (2016).
- [7] Shen, J. et al. Nematic topological superconducting phase in Nb-doped Bi_2Se_3 . npj Quant. Mater. **2**, 59 (2017).
- [8] Asaba, T. et al. Rotational symmetry breaking in a trigonal superconductor Nb-doped Bi_2Se_3 . Phys. Rev. X **7**, 011009 (2017).
- [9] Andersen, L., Wang, Z., Lorenz, T. & Ando, Y. Nematic superconductivity in $\text{Cu}_{1.5}(\text{PbSe})_5(\text{Bi}_2\text{Se}_3)_6$. Phys. Rev. B **98**, 220512 (2018).
- [10] Scheurer, M. S., Hoyer, M. & Schmalian, J. Pair breaking in multiorbital superconductors: An application to oxide interfaces. Phys. Rev. B **92**, 014518 (2015).
- [11] Andersen, L., Ramires, A., Wang, Z., Lorenz, T. & Ando, Y. Generalized Anderson’s theorem for superconductors derived from topological insulators. Sci. Adv. **6**, eaay6502 (2020).
- [12] Zinkl, B. & Ramires, A. Sensitivity of superconducting states to the impurity location in layered materials. Phys. Rev. B **106**, 014515 (2022).
- [13] Fu, L. Odd-parity topological superconductor with nematic order: Application to $\text{Cu}_x\text{Bi}_2\text{Se}_3$. Phys. Rev. B **90**, 100509 (2014).
- [14] Kostylev, I., Yonezawa, S., Wang, Z., Ando, Y. & Maeno, Y. Uniaxial-strain control of nematic superconductivity in $\text{Sr}_x\text{Bi}_2\text{Se}_3$. Nat. Commun. **11**, 4152 (2020).
- [15] Tao, R. et al. Direct visualization of the nematic superconductivity in $\text{Cu}_x\text{Bi}_2\text{Se}_3$. Phys. Rev. X **8**, 041024 (2018).
- [16] Kawai, T. et al. Direction and symmetry transition of the vector order parameter in topological superconductors $\text{Cu}_x\text{Bi}_2\text{Se}_3$. Nat. Commun. **11**, 235 (2020).
- [17] Sasaki, S., Segawa, K. & Ando, Y. Superconductor derived from a topological insulator heterostructure. Phys. Rev. B **90**, 220504 (2014).
- [18] Fu, L. & Berg, E. Odd-parity topological superconductors: Theory and application to $\text{Cu}_x\text{Bi}_2\text{Se}_3$. Phys. Rev. Lett. **105**, 097001 (2010).
- [19] Ando, Y. & Fu, L. Topological crystalline insulators and topological superconductors: From concepts to materials. Annu. Rev. Condens. Matter Phys. **6**, 361–381 (2015).
- [20] Sera, Y., Ueda, T., Adachi, H. & Ichioka, M. Relation of superconducting pairing symmetry and non-magnetic impurity effects in vortex states. Symmetry **12**, 175 (2020).
- [21] See Supplemental Information for additional data and discussions.

- [22] Odobesko, A. et al. Anisotropic vortices on superconducting Nb(110). Phys. Rev. B **102**, 174502 (2020).
- [23] Kim, H., Nagai, Y., Rózsa, L., Schreyer, D. & Wiesendanger, R. Anisotropic non-split zero-energy vortex bound states in a conventional superconductor. Appl. Phys. Rev. **8**, 031417 (2021).
- [24] Nakayama, K. et al. Observation of two-dimensional bulk electronic states in the superconducting topological insulator heterostructure $\text{Cu}_x(\text{PbSe})_5(\text{Bi}_2\text{Se}_3)_6$: Implications for unconventional superconductivity. Phys. Rev. B **92**, 100508 (2015).
- [25] Galvis, J. A. et al. Tilted vortex cores and superconducting gap anisotropy in 2H-NbSe_2 . Commun. Phys. **1**, 30 (2018).
- [26] Dynes, R. C., Narayanamurti, V. & Garno, J. P. Direct measurement of quasiparticle-lifetime broadening in a strong-coupled superconductor. Phys. Rev. Lett. **41**, 1509–1512 (1978).
- [27] Bagchi, M., Brede, J. & Ando, Y. Observability of superconductivity in Sr-doped Bi_2Se_3 at the surface using scanning tunneling microscope. Phys. Rev. Mater. **6**, 034201 (2022).
- [28] Nagai, Y. Field-angle-dependent low-energy excitations around a vortex in the superconducting topological insulator $\text{Cu}_x\text{Bi}_2\text{Se}_3$. J. Phys. Soc. Jpn. **83**, 063705 (2014).
- [29] Nakayama, K. et al. Nanomosaic of topological Dirac states on the surface of $\text{Pb}_5\text{Bi}_{24}\text{Se}_{41}$ observed by nano-ARPES. Nano Lett. **19**, 3737–3742 (2019).
- [30] Ichioka, M., Hayashi, N., Enomoto, N. & Machida, K. Vortex structure in d-wave superconductors. Phys. Rev. B **53**, 15316–15326 (1996).
- [31] Nagai, Y., Ueno, Y., Kato, Y. & Hayashi, N. Analytical formulation of the local density of states around a vortex core in unconventional superconductors. J. Phys. Soc. Jpn. **75**, 104701–104701 (2006).
- [32] Kaneko, S.-i. et al. Quantum limiting behaviors of a vortex core in an anisotropic gap superconductor. J. Phys. Soc. Jpn. **81**, 063701 (2012).
- [33] Maki, K. Gapless superconductivity. In Parks, R. D. (ed.) Superconductivity, vol. 2, chap. 18, 1035–1105 (Marcel Dekker, 1969).
- [34] Zhang, H. et al. Topological insulators in Bi_2Se_3 , Bi_2Te_3 and Sb_2Te_3 with a single Dirac cone on the surface. Nature Physics **5**, 438–442 (2009).
- [35] Liu, C.-X. et al. Model Hamiltonian for topological insulators. Phys. Rev. B **82**, 45122 (2010).
- [36] Kuntsevich, A. Y. et al. Structural distortion behind the nematic superconductivity in

$\text{Sr}_x\text{Bi}_2\text{Se}_3$. New J. Phys. **20**, 103022 (2018).

[37] Smylie, M. P. et al. Multimodal synchrotron X-ray diffraction across the superconducting transition of $\text{Sr}_{0.1}\text{Bi}_2\text{Se}_3$. arXiv: 2207.13221 (2022).

[38] Kriener, M. et al. Electrochemical synthesis and superconducting phase diagram of $\text{Cu}_x\text{Bi}_2\text{Se}_3$. Phys. Rev. B **84**, 054513 (2011).

Author contributions: Y.A. conceived the experiment and A.R. constructed the theory. M.B., supported by J.B. and Y.A., grew the crystals and performed the measurements and data analysis. M.B., A.R. and Y.A. wrote the manuscript with inputs from J.B.

Competing Interests: The authors declare that they have no competing financial interests.

Correspondence: Correspondence and requests for materials should be addressed to Y.A. (ando@ph2.uni-koeln.de).

Data availability: The data that support the findings of this study are available at the online depository figshare with the identifier **** and Supplementary Information. Source data are provided with this paper.

Supplementary Information for “Rotation of gap nodes in the topological superconductor $\text{Cu}_x(\text{PbSe})_5(\text{Bi}_2\text{Se}_3)_6$ ”

I. SAMPLE CHARACTERIZATION

Figure S1 shows the shielding fractions (SF) of three CPSBS samples that were synthesized from the same batch of PSBS crystals. The STM data obtained on sample S-I and on sample S-II is shown in the main text and the data on sample S-III is presented in this supplement. Samples S-I to S-III show a bulk T_c between 2.5 and 2.6 K.

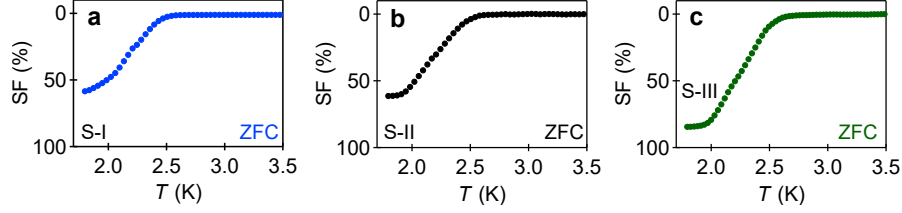


FIG. S1. (a,b,c) Zero-field-cooled (ZFC) magnetization data showing shielding fractions of 59% for Sample S-I (a), 61% for Sample S-II (b) and 84% for Sample S-III (c).

II. SUPPLEMENTAL DATA FOR SAMPLE S-I

The superconducting regions of sample S-I clearly show the structural 1D stripe [Fig. S2(a)], allowing the determination of the monoclinic a and b axis. The monoclinic a axis in this sample is about 145° with respect to the horizontal axis [Fig. S2(b)]. The spatially averaged superconducting gap measured in this region is shown in Fig. S2(c) (same data as Fig. 2(a) of the main text). Moreover, we have experimentally ascertained that the T_c in this region is lower than 1.7 K.

When the external magnetic field is applied normal to the surface, a nearly hexagonal vortex lattice is clearly resolved [Fig. S2(e-g)]. We extrapolate the upper critical field at the surface to about 0.4 T from the magnetic-field dependence of the zero-bias conductance (ZBC) as shown in Fig. S3(d).

We note considerable variations among the shape of different vortices in Fig. S2(e-g), but as discussed in the main text, on average, vortices are elongated roughly at 55° from the horizontal (i.e. at 90° with respect to the a -axis).

III. SUPPLEMENTAL DATA FOR SAMPLE S-II

We characterized the vortex area of sample S-II by taking low-resolution STS-grids in various magnetic fields, as shown in Fig. S3(a-g). The vortex lattice clearly evolves with the magnetic field until the superconductivity is fully suppressed at around ~ 1 T. At low fields, a nearly triangular lattice is observed, in which the distance d_{vortex} between nearest-neighbors is given as $d_{\text{vortex}} \approx 1.075 (\Phi_0/B)^{1/2}$. We plot the average distance between the vortices for varying magnetic fields together with the profile expected for a triangular lattice in Fig. S3(h). We extract the superconducting (SC) gap at each field by averaging the spectra in-between the vortices for a small bias range around E_F . These spectra change systematically as a function of the magnetic field [Fig. S3(i)]. The magnetic-field dependence of the zero-bias conductance (ZBC) normalized to that at 0 T is shown in Fig. S3(j).

The temperature dependence of the SC gap spectra was measured up to the fridge temperature T_{fridge} of 1.7 K [Fig. S3(k)]. Since the effective base temperature of 0.7 K calibrated for $T_{\text{fridge}} = 0.35$ K suggests that the noise in our STM system heats the electrons by $T_{\text{noise}} \simeq 0.35$ K, we fix $T_{\text{eff}} = T_{\text{fridge}} + 0.35$ K when we fit the spectra with the anisotropic gap function discussed in the main text. We can calculate the average gap $\langle \Delta \rangle = \Delta_0 + (2/\pi)\Delta_1$ from the Δ_0 and the Δ_1 values obtained from the fits of the spectra, and the result is plotted in Fig. S3(l) as a function of temperature.

S-I, region I

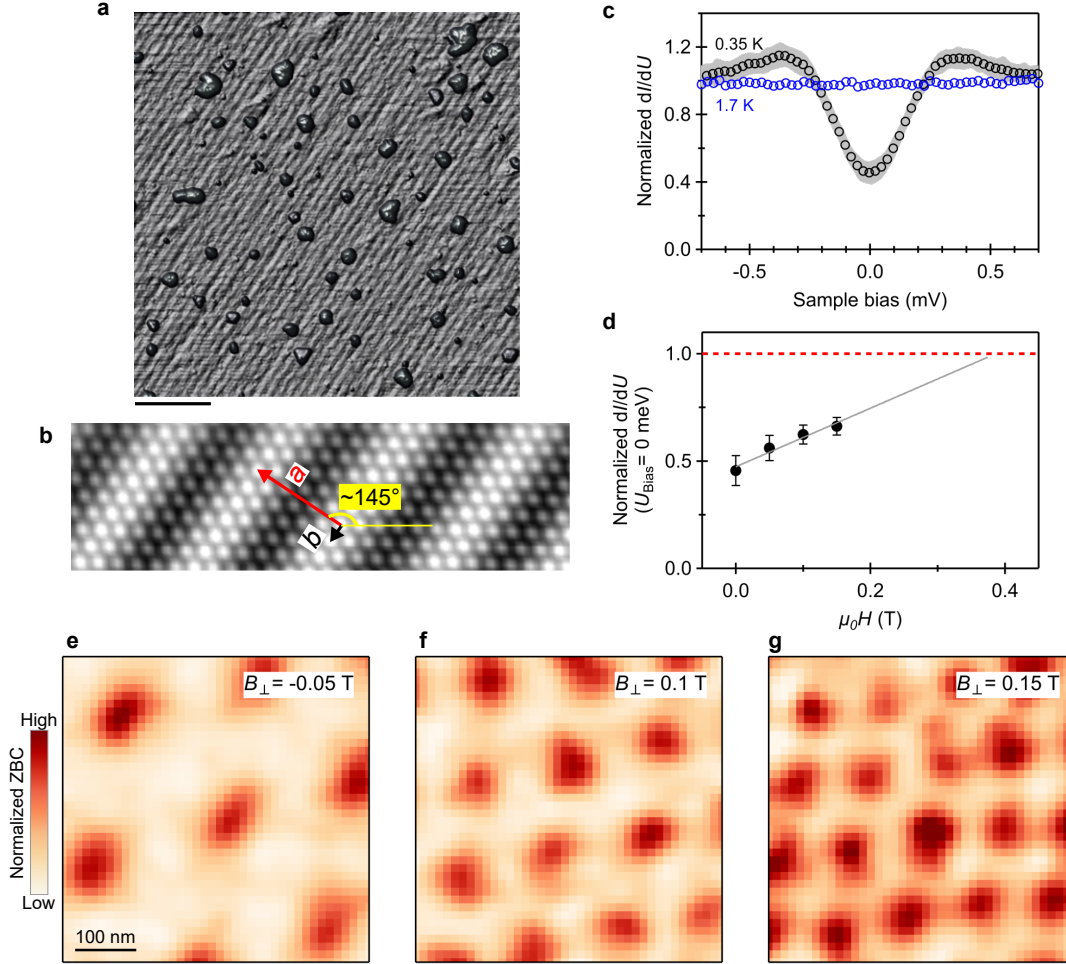


FIG. S2. (a) Pseudo 3D representation of an STM topograph on the SC area of sample S-I. Scale bar corresponds to 20 nm. The structural 1D stripe is clearly observed in the region together with islands/clusters of Cu atoms. (b) Fourier-filtered atomic resolution image taken in the area as in (a) with the monoclinic a and b axes indicated. The a axis is at an angle of about 145° with respect to the horizontal axis for *as-acquired data*. (c) Normalized dI/dU spectra acquired in the region in (a) for a fridge temperatures of 0.35 K (gray open circles) and 1.7 K (blue open circles). The data points correspond to a spatial average of 100 STS over $500 \times 500 \text{ nm}^2$. The light gray area is the standard deviation of the data, as described in the text. (d, e, f, g) Magnetic-field dependence of the normalized ZBC values (d) as obtained from the the zero field grid and grids taken in the presence of a magnetic field [presented in (e - f)]. Red dashed line corresponds to the normal-state conductance. Error bars in (d) correspond to the one sigma standard deviation of the ZBC value of the respective grid. Scan/stabilization parameters: (a) $U = 900 \text{ V}$, $I = 100 \text{ pA}$; (b) $U = 900 \text{ V}$, $I = 200 \text{ pA}$; (e, f, g) $U = 5 \text{ mV}$, $I = 500 \text{ pA}$ (e, f) $I = 100 \text{ pA}$ (g).

IV. FITTING VORTEX PROFILES WITH THE GINZBURG-LANDAU DERIVED EXPRESSION

Zero bias conductance (ZBC) profiles across vortex cores in STM experiments are commonly analyzed [1, 2] with the Ginzburg-Landau (GL) derived expression for the superconducting order parameter,

$$\sigma(r, 0) = \sigma_0 + (1 - \sigma_0) \left(1 - \tanh \left[r / (\sqrt{2} \xi_{\text{GL}}) \right] \right), \quad (\text{S1})$$

where σ_0 is the normalized ZBC away from a vortex centre and r is the distance to the vortex core centre. In Fig. S4 we plot line cuts of the vortex cores discussed in Fig. 1 of the main text together with the fit of the raw data to Eq. (S1). The r -dependences of the ZBC in sample S-I does not really follow Eq. (S1), but from this analysis we obtain ξ_{GL} of about 28 (47) nm for the short (long) axis of the vortex in sample S-I [Fig. S4 (a)] and about 20 (35) nm in S-II [Fig. S4 (b)]. The values are in reasonable agreement with the estimate of ξ_{GL}

S-II, region I

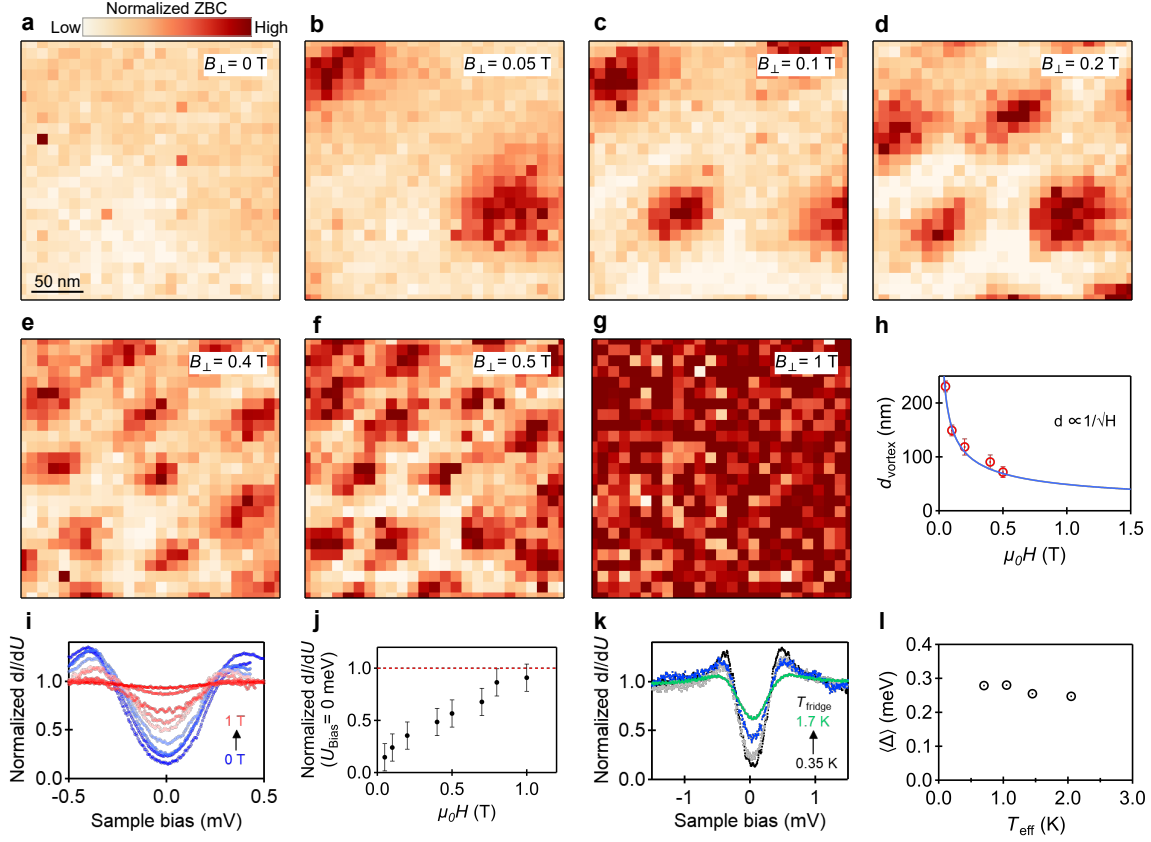


FIG. S3. (a)-(g) Normalized ZBC maps showing the evolution of the vortex lattice in a field of view of 250 nm by 250 nm under various out-of-plane magnetic fields as indicated. The spectrum at each grid point was obtained in the I - V mode. Stabilization parameters: $U = 3$ mV, $I = 50$ pA (100 sweeps). A majority of the vortices are oriented along one direction in all cases. (h) The distance between vortices plotted as a function of the applied magnetic field. The blue curve shows the simulated profile assuming a perfect triangular lattice; deviation of the data points from the simulation curve indicates imperfect ordering. Error bars are given by the larger of the resolution of our STS grid (~ 10 nm) or the standard deviation of the nearest-neighbour distance of all lattice points in the field of view. (i) Normalized dI/dU spectra for various magnetic fields; the curves are obtained by averaging over the grids that lie outside the vortices; the plotted spectra correspond to 0, 0.05, 0.1, 0.2, 0.4, 0.5, 0.7, 0.8, and 1.0 T. (j) Magnetic-field dependence of the normalized ZBC values obtained from the data in (i); the red dashed line signifies the normal-state conductance. Errors bars correspond to a fixed value which is the standard deviation of the ZBC obtained from the zero field grid. (k) SC gap spectra measured in zero field at the fridge temperatures of 0.35, 0.7, 1.1 and 1.7 K; the black curve is also shown in Fig. 2 of the main text. (l) The average gap $\langle \Delta \rangle$ calculated from the Δ_0 and Δ_1 values obtained from the fits to the data in (k) plotted against the effective temperature.

for sample S-I (S-II) based on the measured upper critical field $H_{c2} \approx 0.4$ T (1 T),

$$\xi_{\text{GL}} = \sqrt{\frac{\Phi_0}{2\pi\mu_0 H_{c2}}} \approx 40 \text{ nm (18 nm)},$$

with Φ_0 the (superconducting) magnetic flux quantum and μ_0 the vacuum permeability.

V. EXTENDED DATA FOR FIG. 1 OF THE MAIN TEXT

Here, we give extended data for Fig. 1 of the main text consisting of the unsmoothed ZBC maps, the lattice vectors of the vortex lattice, and the comparison of the average vortex profile based on the analysis of smoothed data as discussed in the main text with the results obtained by fitting the raw data to Eq. (S1).

We determine the vortex lattice for each ZBC map by calculating the centre of every area of the map that exceeds an appropriate threshold value of the ZBC (typically about 0.5). From all lattice points we then determine the three average lattice vectors (\mathbf{a}_1 , \mathbf{a}_2 and \mathbf{a}_3). The results of this procedure are superimposed onto the raw data in Fig. S5 (b) and (e). Interestingly, we find that the hexagonal vortex lattice observed in sample S-I is compressed along the vortex lattice vector \mathbf{a}_3 by about 15 to 20%. Moreover, the vortex lattice

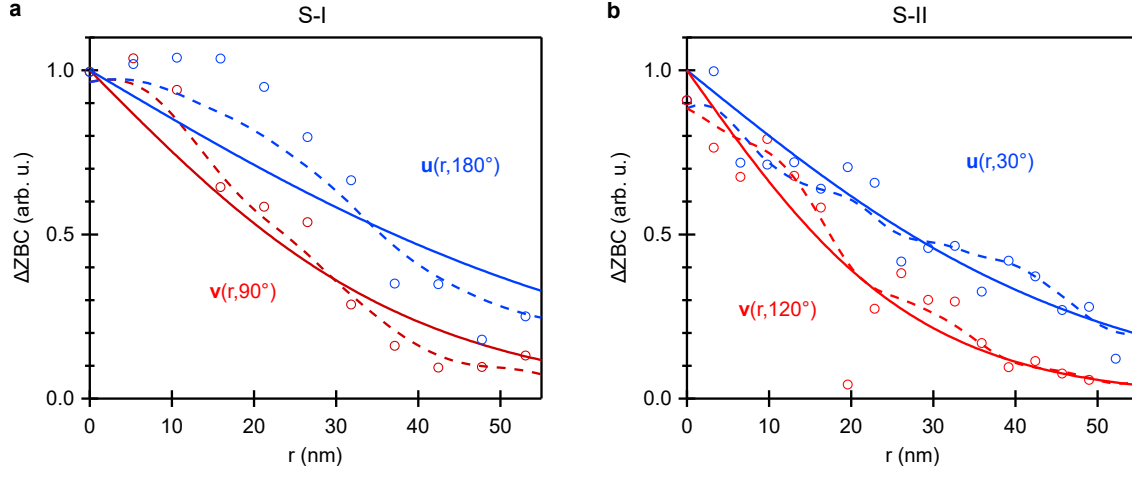


FIG. S4. (a) Line profiles of the vortices taken from Fig. 1(e) of the main text. Open circles, dashed lines, and solid lines refer to raw data, smoothed curve, and GL fits to Eq. (S1), respectively. The smoothing was performed for the analysis of the half width at half maximum mentioned in the text by using a standard Gaussian filter with the smallest (3×3 pixels) kernel with up to three iterations. Blue (red) data are taken along the major (minor) vortex axis; note that the images in Fig. 1(a,b) of the main text are rotated clockwise by 55° to align the monoclinic a -axis with the vertical axis. (b) The same as (a) but for line profiles shown in Fig. 1(g) of the main text. The GL fit gives $\xi_{GL} = 28 \pm 2$ nm (47 ± 6 nm) for the short (long) axis for the vortex of sample S-I and 20 ± 2 nm (35 ± 2 nm) for the vortex of sample S-II.

(\mathbf{a}_2) is rotated by about 10 to 15° with respect to the crystallographic a -axis. We conservatively estimate the experimental uncertainty due to thermal drift and piezoelectric creep as 10% for the compression and 10° for the rotation. We leave the exploration of the origin of this interesting vortex lattice deformation for future studies.

Instead, we analyze the vortex shape at each lattice site by taking line profiles as a function of polar angle and determine ξ (defined as the half width at half maximum) from smoothed data and ξ_{GL} by fitting the raw data to Eq. (S1) as shown in Fig. S4. We numerically average $\xi_{GL}(\varphi)$ (and $\xi(\varphi)$) of all lattice sites and plot the results in Fig. S5 (c) and (f) for the vortex lattice at 0.15 and 0.2 T, respectively. On the one hand, we observe considerable variations in the vortex shape between different lattice sites, which likely reflects differences in the local scattering potential; on the other hand, a clear two-fold symmetry with a minimal average vortex extension parallel to the a -axis is apparent. Comparing $\langle \xi_{GL} \rangle$ and $\langle \xi \rangle$ we find the same qualitative behavior.

As mentioned above, we observed significant variations in the vortex shape anisotropy between different lattice sites in sample S-I. Therefore, to achieve a high level of confidence in the determination of the vortex elongation axis, we have analyzed a relatively large number of ZBC maps at 0.15 and 0.2 T which are shown in Fig. S6 and Fig. S7, respectively. The data shown in Fig. 1 (f) of the main manuscript is the average of all the lattice sites indicated in Fig. S6 and Fig. S7.

The same analysis as discussed for sample S-I above was also performed for the vortex lattice observed in sample S-II which is shown in Fig. 1 (c) and (e) of the main text. The results are shown in Fig. S8. On the one hand, we observe a rotation of lattice vector \mathbf{a}_2 of -15 to -23° with respect to the crystallographic a -axis, which is clearly different from the orientation observed for sample S-I; on the other hand, the entire vortex lattice in S-II is noticeably distorted (likely due to disorder related pinning of vortices) and does not allow for a meaningful analysis of the vortex lattice anisotropy.

The vortex shape analysis performed at each lattice site yields the average $\langle \xi_{GL} \rangle$ and $\langle \xi \rangle$ respectively plotted for 0.2 and 0.4 T in Fig. S8 (c) and (f). The noticeably smaller standard deviations compared to the data obtained for sample S-I is likely attributed to reduced vortex lattice motion due to the pinning centers and less thermal smearing due to the larger superconducting gap. Regardless of the origin, most vortices in sample S-II have similar elliptical shape with the same orientation of the major axis which is about 60° rotated with respect to the crystallographic a -axis and clearly different from the orientation observed in sample S-I.

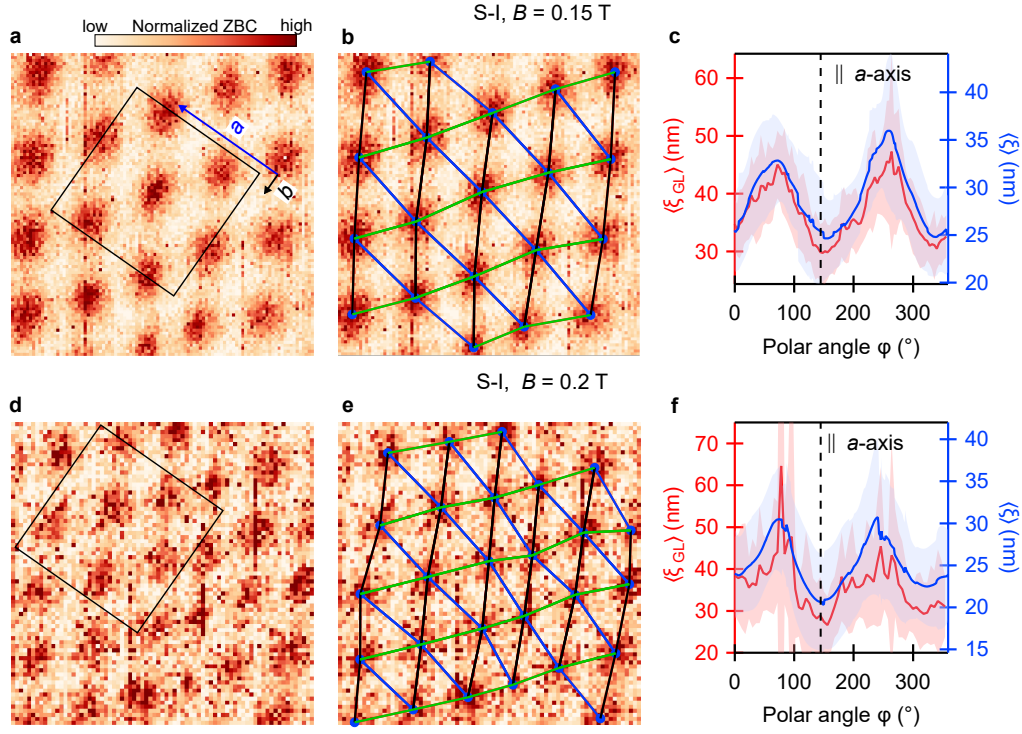


FIG. S5. (a) Larger region of the vortex lattice in sample S-I in the out-of-plane magnetic field of $B = 0.15$ T. The black square indicates the data show in Fig. 1(a) of the main text. The monoclinic a -axis and b -axis are given. The vortex lattice in the field of view of $500 \text{ nm} \times 500 \text{ nm}$ is determined and the results are superimposed onto the raw data in (b). Blue dots mark the lattice points corresponding to vortex centres. The lattice vectors \mathbf{a}_1 (black), \mathbf{a}_2 (blue), \mathbf{a}_3 (green) are indicated and their average lengths are $|\mathbf{a}_1| = (133 \pm 8) \text{ nm}$, $|\mathbf{a}_2| = (138 \pm 9) \text{ nm}$ and $|\mathbf{a}_3| = (111 \pm 7) \text{ nm}$. The average angle between \mathbf{a}_2 and the monoclinic a -axis is $\angle_{\mathbf{a}_2, a} = (12 \pm 4)^\circ$. Line profiles of the normalized ZBC are taken as a function of the polar angle φ at each lattice point and the GL in-plane coherence length is determined by fitting the raw data to Eq. (S1). (c) The average $\langle \xi_{GL} \rangle$ of all lattice points is plotted in red, where the light shaded region indicates the standard deviation. For comparison, the average vortex core radius $\langle \xi \rangle$, which is determined from the half width at half maximum of the smoothed data as discussed in the main text, is shown in blue. (d,e,f) The same analysis as in (a,b,c) for the vortex lattice in 0.2 T shown in Fig. 1(b) of the main text. The vortex lattice parameters for (e) are: $|\mathbf{a}_1| = (113 \pm 7) \text{ nm}$, $|\mathbf{a}_2| = (116 \pm 9) \text{ nm}$, $|\mathbf{a}_3| = (94 \pm 13) \text{ nm}$ and $\angle_{\mathbf{a}_2, a} = (15 \pm 6)^\circ$.

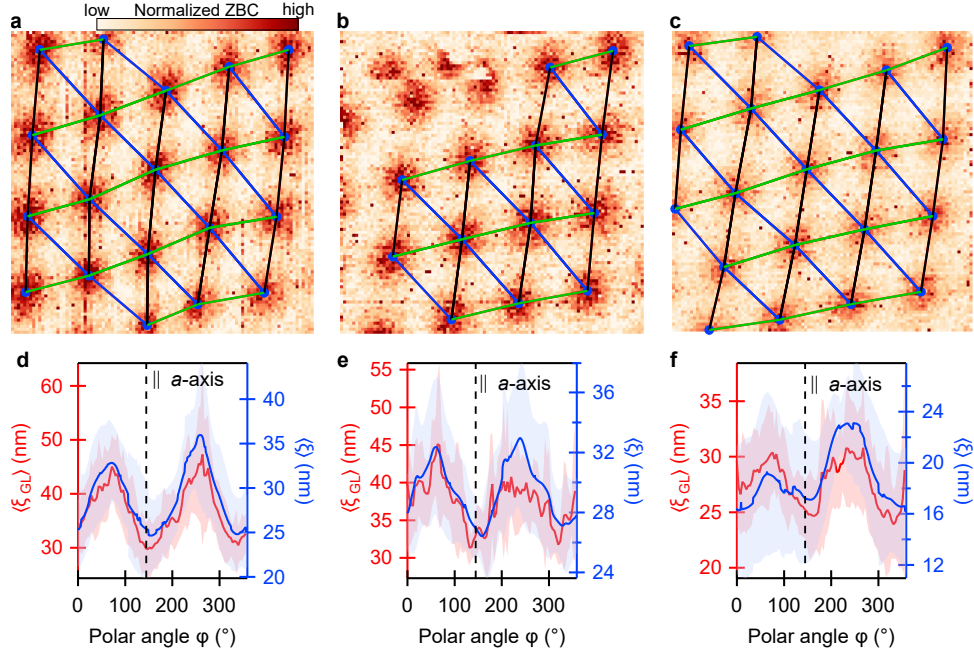


FIG. S6. All the data of the vortices in sample S-I in the out-of-plane magnetic field of $B = 0.15$ T used for the averaging to generate Fig. 1(f) of the main text. Panels (a,d) are the same as those shown in Fig. S5(b,c). The field of view of panels (b) and (c) is $500 \text{ nm} \times 500 \text{ nm}$, and the data are analysed and presented in the same way as in Fig. S5(b,c). Vortex lattice parameters: $|\mathbf{a}_1| = (133 \pm 5) \text{ nm}$, $|\mathbf{a}_2| = (145 \pm 4) \text{ nm}$, $|\mathbf{a}_3| = (114 \pm 5) \text{ nm}$ and $\angle_{\mathbf{a}_2, \mathbf{a}} = (13 \pm 3)^\circ$ for (b); $|\mathbf{a}_1| = (132 \pm 10) \text{ nm}$, $|\mathbf{a}_2| = (140 \pm 7) \text{ nm}$, $|\mathbf{a}_3| = (119 \pm 7) \text{ nm}$ and $\angle_{\mathbf{a}_2, \mathbf{a}} = (12 \pm 3)^\circ$ for (c).

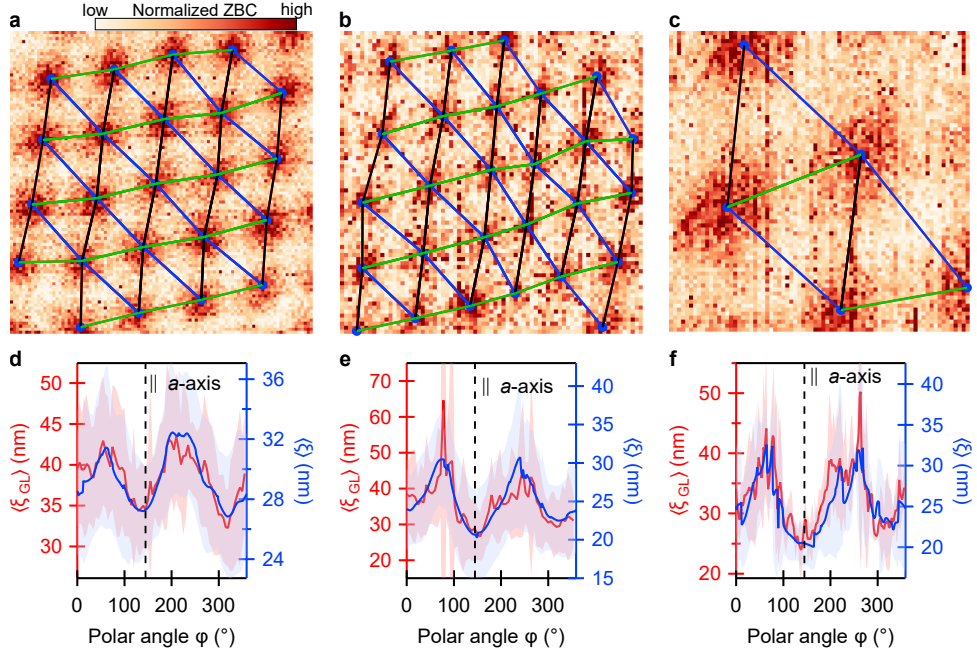


FIG. S7. All the data of the vortices in sample S-I in the out-of-plane magnetic field of $B = 0.2$ T used for the averaging to generate Fig. 1(f) of the main text. Panels (b,e) are the same as those shown in Fig. S5(e,f). The field of view of panels (a) and (c) is $500 \text{ nm} \times 500 \text{ nm}$ and $200 \text{ nm} \times 200 \text{ nm}$, respectively. The data are analysed and presented in the same way as in Fig. S5(e,f). Vortex lattice parameters: $|\mathbf{a}_1| = (108 \pm 3) \text{ nm}$, $|\mathbf{a}_2| = (124 \pm 7) \text{ nm}$, $|\mathbf{a}_3| = (105 \pm 4) \text{ nm}$ and $\angle_{\mathbf{a}_2, \mathbf{a}} = (10 \pm 4)^\circ$ for (a); $|\mathbf{a}_1| = (107 \pm 3) \text{ nm}$, $|\mathbf{a}_2| = (109 \pm 6) \text{ nm}$, $|\mathbf{a}_3| = (94 \pm 6) \text{ nm}$ and $\angle_{\mathbf{a}_2, \mathbf{a}} = (11 \pm 5)^\circ$ for (c).

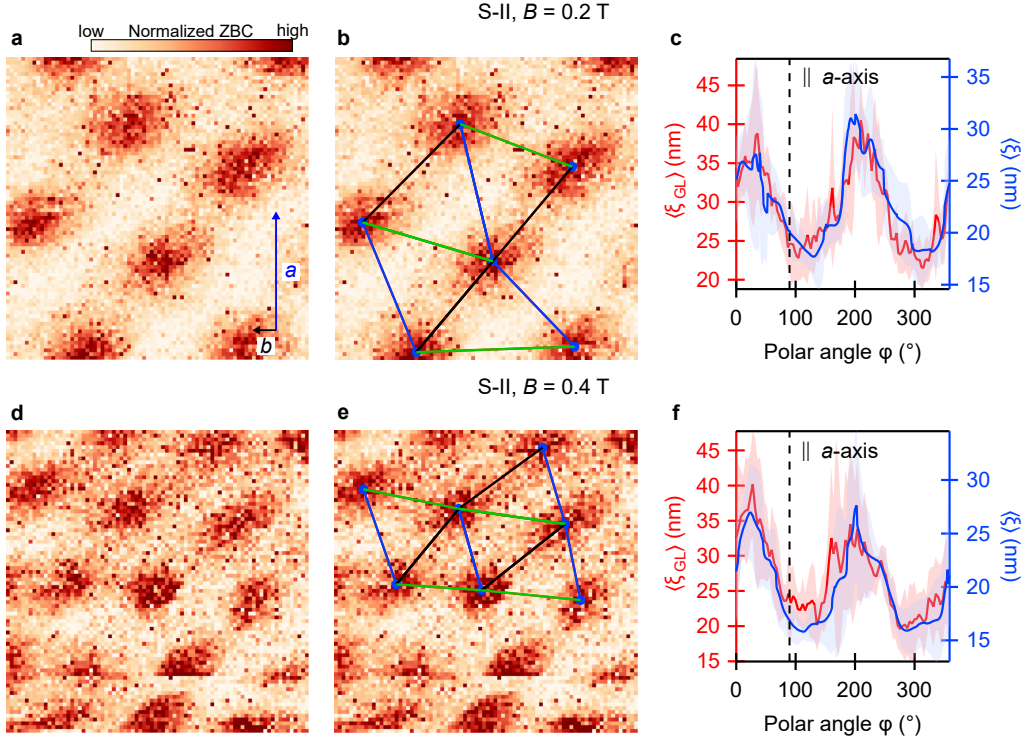


FIG. S8. (a,b) The vortex lattice in sample S-II in the out-of-plane magnetic field of $B = 0.2$ T show in Fig. 1(c) of the main text. The vortex lattice in the field of view of $250 \text{ nm} \times 250 \text{ nm}$ is determined and the results are superimposed onto the raw data in (b). Blue dots mark the lattice points corresponding to vortex centres. The lattice vectors \mathbf{a}_1 (black), \mathbf{a}_2 (blue), \mathbf{a}_3 (green) are indicated and their average lengths are $|\mathbf{a}_1| = (105 \pm 8) \text{ nm}$, $|\mathbf{a}_2| = (113 \pm 10) \text{ nm}$ and $|\mathbf{a}_3| = (115 \pm 13) \text{ nm}$. The average angle between \mathbf{a}_2 and the monoclinic a -axis is $\angle_{\mathbf{a}_2, a} = (-23 \pm 15)^\circ$. Line profiles of the normalized ZBC are taken as a function of the polar angle φ at each lattice point and the GL in-plane coherence length is determined by fitting the raw data to Eq. (S1). (c) The average $\langle \xi_{GL} \rangle$ is plotted in red, where the light shaded region indicates the standard deviation. For comparison, the average vortex core radius $\langle \xi \rangle$, which is determined from the smoothed data as discussed in the main text, is shown in blue. (d-f) The same analysis as in (a-c) for the vortex lattice in 0.4 T shown in Fig. 1(d) of the main text. The vortices shown here are used for the averaging to generate Fig. 1(h) of the main text. The vortex lattice parameters for (e) are $|\mathbf{a}_1| = (86 \pm 4) \text{ nm}$, $|\mathbf{a}_2| = (72 \pm 8) \text{ nm}$, $|\mathbf{a}_3| = (83 \pm 8) \text{ nm}$ and $\angle_{\mathbf{a}_2, a} = (-15 \pm 3)^\circ$.

VI. INFLUENCE OF THE IN-PLANE MAGNETIC FIELD ON THE VORTEX ELONGATION

To dismiss the possibility that the observed vortex elongation is a mere consequence of a magnetic field that is not exactly out-of-plane but is tilted away from the z axis, we performed the following experiment: We applied an intentional in-plane magnetic field of the magnitude of 35 mT with the azimuthal angle of 40° and 130° . The resultant magnetic field is $\sim 10^\circ$ off from the z axis. As shown in Fig. S9, we did not observe any noticeable change in the vortex anisotropy in spite of the intentional misalignment of the field. Also, the averaged orientation of the vortices did not change upon rotating the in-plane component within the experimental uncertainty of about 10° .

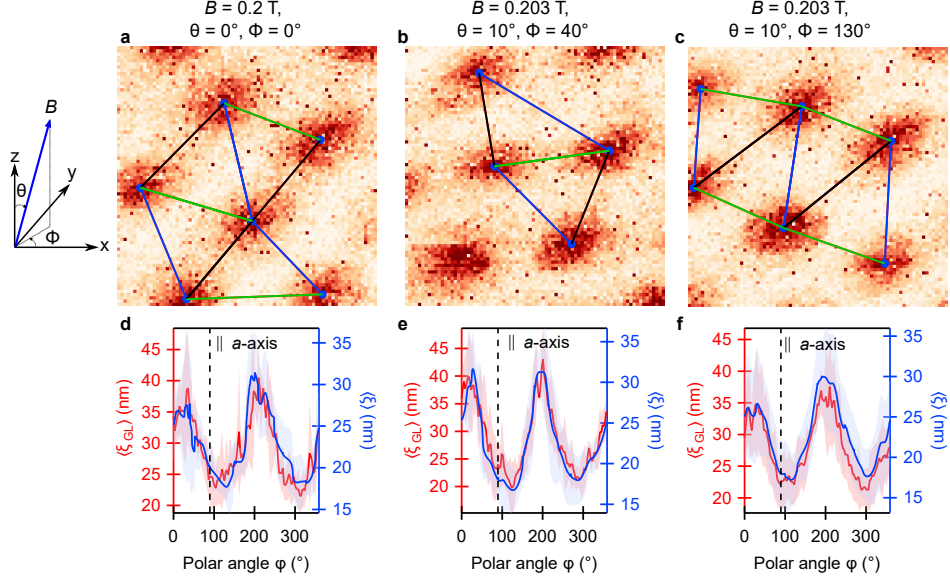


FIG. S9. (a) Normalized ZBC maps in the perpendicular magnetic field of 0.2 T ($\theta = 0^\circ$). (b,c). An additional in-plane magnetic field of 35 mT applied in the direction of $\phi = 40^\circ$ (b) and $\phi = 130^\circ$ (c); these in-plane magnetic fields cause θ to become 10° with the total magnetic field of 0.203 T. The definition of θ and ϕ is shown on the left. Stabilization parameters: $U = 1$ mV, $I = 50$ pA and $U_{\text{mod}} = 100 \mu\text{V}_p$. (d,e,f) The average $\langle \xi_{GL} \rangle$ and $\langle \xi \rangle$ calculated from the lattice sites indicated by blue dots in (a,b,c). Note that the panels (a,d) are the same as Fig. S8(b,c).

VII. ABSENCE OF VORTEX BOUND STATES

No Caroli-de Gennes-Matricon states were observed in the core of a single isolated vortex in CPSBS (Fig. S10). The absence of bound states in the vortex core is expected for a dirty superconductor [3]. Based on the values for residual resistivity (ρ_0) and carrier density (n) in Ref. [4], we estimate the mean free path (l) in our sample [$l = \hbar k_F / (\rho_0 n e^2)$] to be on the order of only a few nanometer, while the average in-plane coherence length (ξ_{GL}) is measured to be about 25 nm, i.e., CPSBS is a dirty superconductor. Importantly, despite being in the dirty limit, a clear anisotropy in the vortex shape is observed.

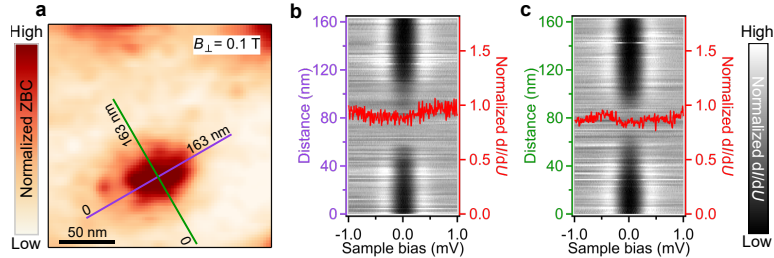


FIG. S10. (a) Normalized ZBC map at $B_\perp = 0.1$ T showing a single isolated vortex. (b) Normalized dI/dU spectra along the purple line (long axis) in (a). Each horizontal row is a dI/dU spectrum vs sample bias. The color scale represents the dI/dU intensity and the vertical axis corresponds to the distance along the purple line in (a). The red dI/dU spectrum superimposed on the map is taken at the center of the vortex and highlights the absence of any vortex bound states. (c) A similar map as done in (b) for the green line (short axis) in (a), clearly illustrating the vortex anisotropy. Stabilization parameters: $U = 1$ mV, $I = 50$ pA (100 sweeps) for (a); $U = 3$ mV, $I = 50$ pA (200 sweeps) for (b) and $U = 3$ mV, $I = 50$ pA (200 sweeps) for (c).

VIII. STATISTICAL OVERVIEW OF THE SC REGIONS OBSERVED BY STM ON THE SURFACE

Tao *et al.* [5] reported that the probability to find SC regions on the surface of $\text{Cu}_x\text{Bi}_2\text{Se}_3$ was less than 5% in their STM study. Our experience was similar during the scanning on the surface of CPSBS. It is more common to find non-superconducting areas. In our experiments a single scan area corresponds to $1.5\text{ }\mu\text{m}$ by $1.5\text{ }\mu\text{m}$, which is the maximum range for the scan piezo. A new scan area on the sample is accessed by moving the sample stage with respect to the tip holder. In Table I, we show the total number of scan areas along with the number of areas in which SC was observed. By multiplying the number of scan areas with the area of a single scan frame, we estimate a SC area of $6.75\text{ }\mu\text{m}^2$ out of $13.5\text{ }\mu\text{m}^2$ in sample S-I, $6.8\text{ }\mu\text{m}^2$ out of $65\text{ }\mu\text{m}^2$ in sample S-II and $11.3\text{ }\mu\text{m}^2$ out of $63\text{ }\mu\text{m}^2$ in sample S-III.

We previously reported for $\text{Sr}_x\text{Bi}_2\text{Se}_3$ [6] that spurious superconducting gap was often observed due to picking up of a superconducting material on the tip from the sample, and it was also the case in CPSBS. Identification of a boundary between a superconducting and non-superconducting region with the same tip apex conditions was used as the criteria for ascertaining a superconducting gap to reside on the sample side, rather than on the tip side.

Sample	Number of scan areas	Number of SC regions
S-I	6	3
S-II	29	3
S-III	28	5

TABLE I. Summary of total number of regions scanned and number of SC regions found on three CPSBS samples.

IX. SPATIAL VARIATION OF THE SUPERCONDUCTING GAP SPECTRUM

In Fig. S11 we give an overview of the superconducting gaps measured for the various superconducting regions observed in the three different samples S-I, S-II and S-III (see also Table I). For each region, a large-area spectroscopy grid was evaluated. The open black circles and the light gray shaded area give the arithmetic mean ($\bar{x} = \sum_{i=1}^n X_i/n$) and the corresponding standard deviation ($\text{SD} = \sqrt{\frac{\sum_{i=1}^n (x_i - \bar{x})^2}{(n-1)}}$), respectively. One can see that when there is a large ZBC, the data can be reasonably fit with both the nodal (blue trace) and the anisotropic (red trace) gap functions discussed in the main text. We observe significant variations of the gap magnitude, which is presumably due to differences in local Cu-concentration and/or electric field induced weakening of superconductivity [6].

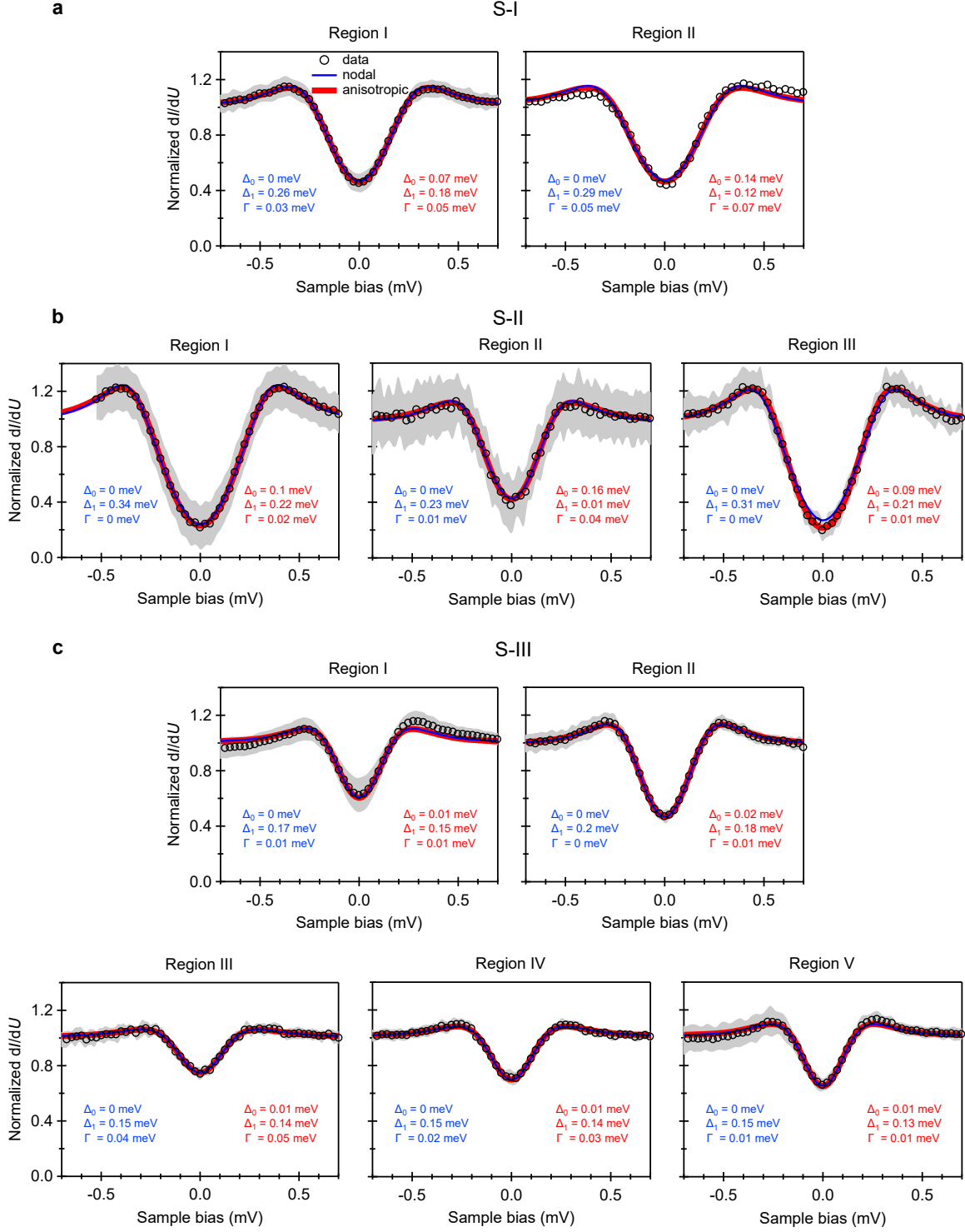


FIG. S11. Variations in the superconducting gap observed in samples S-I, S-II, and S-III. For each region we show the spatial average (black open circles) and the corresponding standard deviation (light gray area). The spatial average is obtained by numerically averaging 100 STS over 500 by 500 nm², 900 STS over 300 by 300 nm², 60 STS over 25 by 500 nm², 28 STS over 50 by 500 nm², 1600 STS over 500 by 500 nm², 80 STS over 20 by 1500 nm², 200 STS over 40 by 500 nm², 50 STS over 25 by 1400 nm², 300 STS over 500 by 500 nm², for region I (sample S-I), region I – III (sample S-II), and region I – V (sample S-III), respectively. For region II of sample S-I, a point STS is shown. The blue and red traces correspond to the nodal and anisotropic fit to the data, respectively, as described in the text. Stabilization parameters: $U = 1.5$ to 5 mV, $I = 50$ or 500 pA.

X. ORIENTATION OF SUPERCONDUCTING GAP MINIMA ON SAMPLE S-III SURFACE

Similar to sample S-II, no structural stripe pattern was observed in sample S-III (see Sec. XI). Moreover, the smaller SC magnitude paired with significant spatial inhomogeneity prohibited a reliable evaluation of the anisotropy of superconducting vortices. Due to this difficulty, we probed the anisotropy in the superconducting gap of region II of sample S-III by measuring the response to an in-plane magnetic field (B_{\parallel}) of 0.25 T, a technique used for $\text{Cu}_x\text{Bi}_2\text{Se}_3$ by Tao *et al.* [5]. When the magnetic field is rotated by an angle φ in the ab -plane of the crystal, the gap spectra show a clear variation [Fig. S12(a,b)].

The influence of B_{\parallel} on the zero-energy DOS was calculated within the Kramer–Pesch approximation by Nagai [7] and the result is in good agreement with our experimental data [Fig. S12(b)]. From this comparison, one can identify the orientation of the gap minima with respect to the crystallographic axes in Fig. S12(c) and compare it to the orientation of the gap minima observed in sample S-I and S-II. The orientation of the gap minima in sample S-III is close to that in sample S-II and is off by only $\sim 10^\circ$. In this regard, it is useful to note that Tao *et al.* [5] reported a rotation of the gap minima by up to 20° away from the zero-field position when the in-plane magnetic field was applied. It is likely that the same effect is observed here.

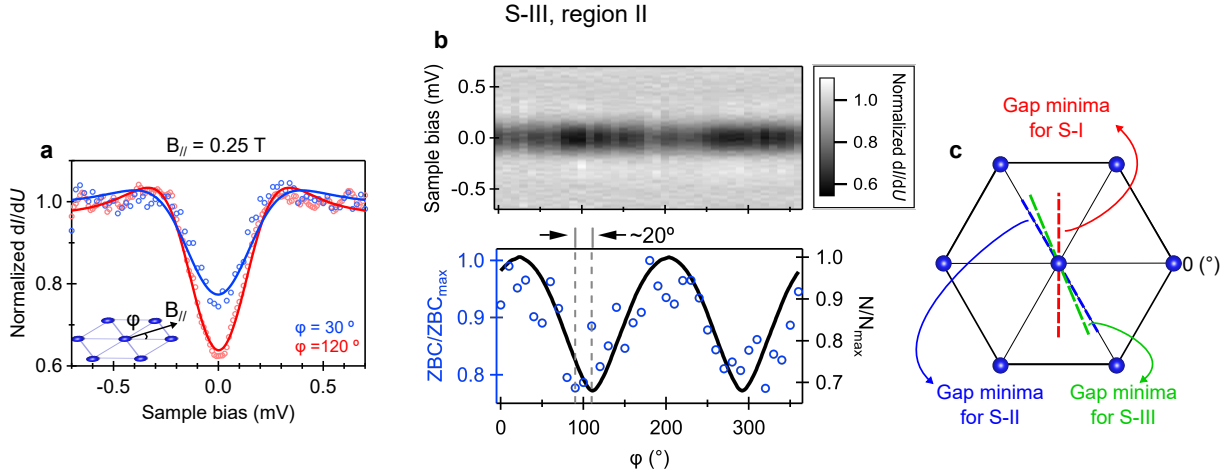


FIG. S12. (a) Point STS taken in region II of sample S-III, but in the presence of an in-plane magnetic field (B_{\parallel}) of 0.25 T for different field orientations (φ). The definition of φ is indicated in the inset. Solid lines are fits to the data. Here, the measured superconducting gaps are fit using Γ as the only fitting parameter; $T_{\text{eff}} = 0.7$ K, $\Delta_0 = 0.02$ meV and $\Delta_1 = 0.18$ meV are fixed. (b) A twofold oscillation is clearly visible in the raw data of dI/dU at zero bias (top) and this angular dependence of the zero-bias DOS can be fit with the changes in zero energy DOS (N) calculated by Nagai [7] (bottom) to quantify the minima at approximately 110° and 290° . (c) The positions of the minima in the superconducting gap structure obtained for samples S-I (red dashed line), S-II (blue dashed line) and S-III (green dashed line). Stabilization parameters: (a,b) $U = 1.5$ mV, $I = 100$ pA.

XI. TOPOGRAPHY AND SPECTROSCOPY ON PSBS AND CPSBS

In Fig. S13, we show large scale topography images taken on the surface of PSBS, non-superconducting (NSC) areas of CPSBS, and superconducting areas of CPSBS found on samples S-I, S-II and S-III. The clear 1D stripe on the surface of PSBS becomes more disordered on the NSC surface of CPSBS. The stripe was not observed in the SC regions of S-II and S-III but found on the SC regions of S-I.

The image shown in Fig. S13(h) corresponds to the area where the vortices were observed for S-II. The area was disordered, which made it impossible to obtain clear atomic-resolution images. In comparison, the SC areas on S-I and S-III [Fig. S13(g,i)] are less disordered and atomic-resolution images could be obtained.

We note a correlation between the superconducting gap as discussed in Sec. IX and the amount of (presumably) Cu remaining on the surface. The superconducting region in sample S-III shows few and small clusters [white spots in Fig. S13(i)] and the smallest superconducting gap, S-I exhibits extended and larger clusters [white areas in Fig. S13(g)] and an intermediate superconducting gap and S-II is entirely covered with Cu showing the largest superconducting gap.

We show in Figs. S13(c, f, j) large scale dI/dU spectra taken on the different surfaces. As discussed in the main text, the cleaved surface of PSBS is a single QL of Bi_2Se_3 above the PbSe layer. The ARPES data [8] on this surface show a single, parabolic electron-like band with an onset around ~ -600 meV. The onset of this band is clearly seen in our dI/dU spectrum [Fig. S13(c)], since the LDOS shows a minima exactly around ~ -600 meV.

On the cleaved surface of CPSBS, the ARPES data [9] show two electron-like bands, both 2D in nature, at the onset energies of -600 meV and -280 meV. It is difficult to identify these bands in the spectroscopy curves [Fig. S13(f,j)] due to the significant additional DOS around these energies. Neither is it possible to conclude any shift of the surface bands in comparison to the spectrum on PSBS.

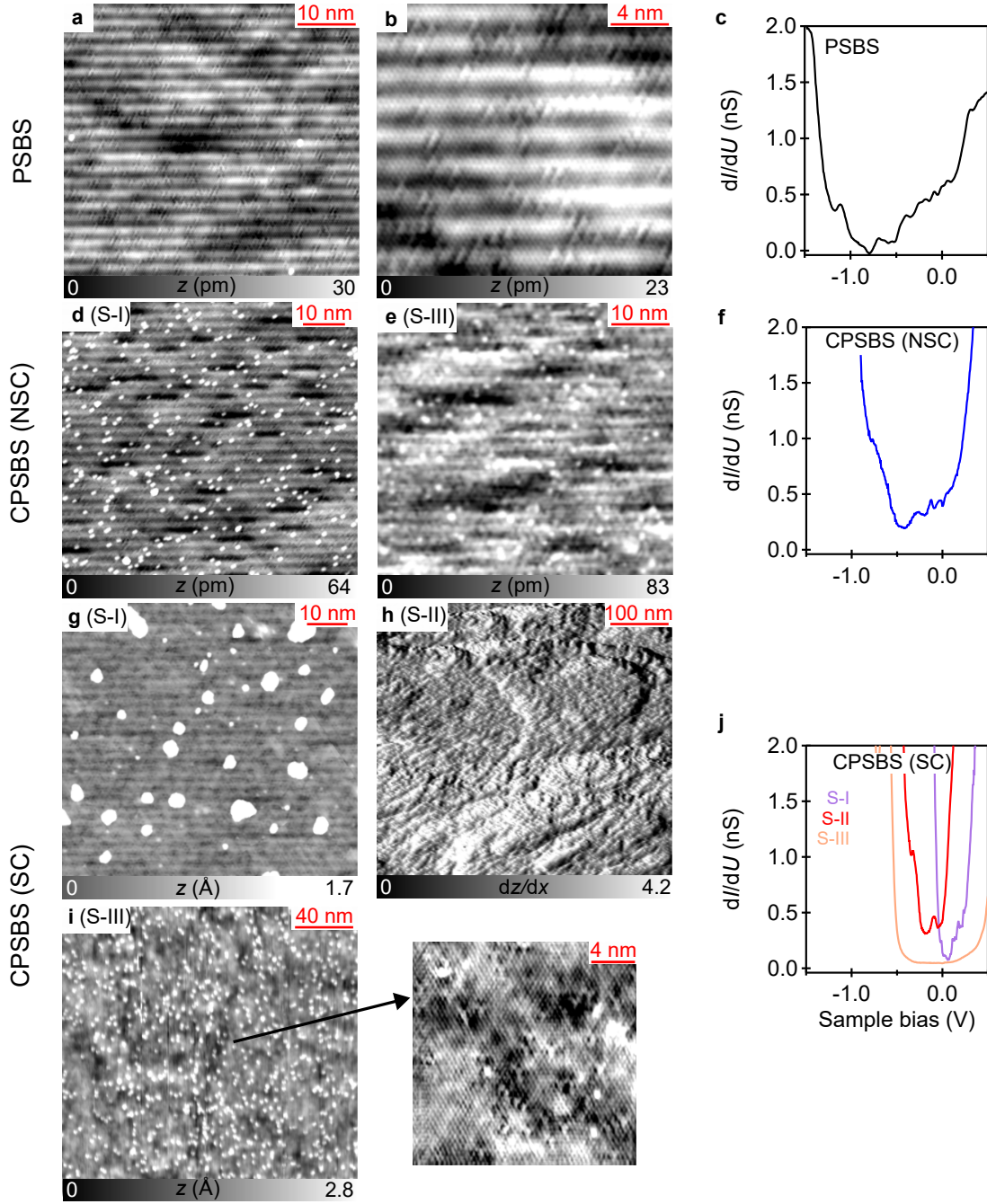


FIG. S13. (a, b, d, e, g, h and i) STM topographs on the cleaved surface of PSBS (a,b), on a non-superconducting surface of CPSBS (d,e), and on a SC area of CPSBS in sample S-I (g), sample S-II (h) and sample S-III (i). The image (h) is a differential image; no atomic-resolution image could be obtained in the SC area of sample S-II due to higher corrugation. However, it was possible to resolve the lattice in the SC area found in S-I and S-III in spite of the significant coverage of Cu clusters. The atomic resolution image for S-III is shown on the right side of (i). (c, f, j) dI/dU spectrum on the surface of PSBS (c), CPSBS (NSC) (f) and CPSBS (SC) (S-I, S-II and S-III) (j). Scan/stabilization parameters: $U = 900$ mV, $I = 20$ nA for (a); $U = 900$ mV, $I = 20$ nA for (b); $U = 500$ mV, $I = 500$ pA for (c); $U = 950$ mV, $I = 50$ pA for (d); $U = -10$ mV, $I = 1$ nA for (e); $U = -900$ mV, $I = 500$ pA for (f); $U = 900$ mV, $I = 100$ pA for (g); $U = 1$ V, $I = 10$ pA for (h); $U = -900$ mV, $I = 500$ pA (right: $U = -5$ mV, $I = 5$ nA) for (i); $U = 500$ mV, $I = 500$ pA (S-I), $U = -600$ mV, $I = 1$ nA (S-II) and $U = -900$ mV, $I = 2$ nA (S-III) for (j).

XII. SYMMETRY ANALYSIS

A. Symmetry of the Bi₂Se₃ quintuple layers

The Bi₂Se₃ quintuple-layer structure is associated with point group D_{3d} [10, 11]. This group consists of twelve symmetry operations organized in six conjugacy classes: \hat{E} , the identity; \hat{P} , inversion; $2\hat{C}_3$: two rotations along the z-axis by $\pm 120^\circ$; $3\hat{C}_2'$: three rotations by 180° along the x-axis and equivalent in-plane axes; $2\hat{S}_6$: rotations by $\pm 60^\circ$ along the z-axis followed by in-plane mirror reflection; $3\hat{\sigma}_d$: three vertical mirrors passing through the yz-plane and equivalent planes. The irreducible representations can be identified from the character table for D_{3d} , as displayed in Table II.

irrep	\hat{E}	$2\hat{C}_3$	$3\hat{C}_2'$	\hat{P}	$2\hat{S}_6$	$3\hat{\sigma}_d$
A_{1g}	+1	+1	+1	+1	+1	+1
A_{2g}	+1	+1	-1	+1	+1	-1
E_g	+2	-1	0	+2	-1	0
A_{1u}	+1	+1	+1	-1	-1	-1
A_{2u}	+1	+1	-1	-1	-1	+1
E_u	+2	-1	0	-2	+1	0

TABLE II. Character table for the point group D_{3d} .

1. Description of the normal state

The normal state Hamiltonian can be described by two effective orbitals of opposite parity, referred as P_{1z+} and P_{2z-} [11, 12]. In the basis $\Phi_{\mathbf{k}}^\dagger = (c_{1\uparrow}^\dagger, c_{1\downarrow}^\dagger, c_{2\uparrow}^\dagger, c_{2\downarrow}^\dagger)_{\mathbf{k}}$, the Hamiltonian can be parametrized as:

$$\hat{H}_0(\mathbf{k}) = \sum_{a,b} h_{ab}(\mathbf{k}) \hat{\tau}_a \otimes \hat{\sigma}_b, \quad (\text{S2})$$

where $\hat{\tau}_{a=1,2,3}$ are Pauli matrices encoding the orbital degrees of freedom (DOF), $\hat{\sigma}_{b=1,2,3}$ are Pauli matrices encoding the spin DOF, and $\hat{\tau}_0$ and $\hat{\sigma}_0$ are two-dimensional identity matrices in orbital and spin space, respectively. In the presence of time-reversal and inversion symmetries, the only allowed terms in the Hamiltonian have the subscripts $(a, b) = \{(0, 0), (2, 0), (3, 0), (1, 1), (1, 2), (1, 3)\}$. Time-reversal symmetry is defined as $\hat{\Theta} = K\hat{\tau}_0 \otimes (i\hat{\sigma}_2)$, where K stands for complex conjugation, and the parity operator as $\hat{P} = \hat{\tau}_3 \otimes \hat{\sigma}_0$. The properties of the $\hat{\tau}_a \otimes \hat{\sigma}_b$ matrices under the point group operations allow us to associate each of these terms to a given irreducible representation of D_{3d} , therefore constraining the momentum dependence of the form factors $h_{ab}(\mathbf{k})$ by symmetry. Table III provides the details on the properties of each term in the normal-state Hamiltonian and an expansion of $h_{ab}(\mathbf{k})$ for small momenta.

(a, b)	\hat{P}	\hat{C}_3	\hat{C}_2'	$\hat{\sigma}_d$	Irrep	$h_{ab}(\mathbf{k})$	Process
(0, 0)	+1	+1	+1	+1	A_{1g}	$C_0 + C_1 k_z^2 + C_2(k_x^2 + k_y^2)$	Intra-orbital hopping
(2, 0)	-1	+1	-1	+1	A_{2u}	$B_0 k_z$	Inter-orbital hopping
(3, 0)	+1	+1	+1	+1	A_{1g}	$M_0 + M_1 k_z^2 + M_2(k_x^2 + k_y^2)$	Intra-orbital hopping
(1, 1)	-1	y	-1	+1	E_u	$-A_0 k_y$	SOC
(1, 2)	-1	x	+1	-1	E_u	$A_0 k_x$	SOC
(1, 3)	-1	+1	+1	-1	A_{1u}	$R_1 k_x(k_x^2 - 3k_y^2)$	SOC

TABLE III. Parametrization of the normal-state Hamiltonian given in Eq. (S2) for materials in the family of Bi₂Se₃. The columns labeled by \hat{P} , \hat{C}_3 , \hat{C}_2' and $\hat{\sigma}_d$ indicate how the basis matrices $\hat{\tau}_a \otimes \hat{\sigma}_b$, indicated by (a, b) , transform under the respective point group operations, such that one can associate these with different irreducible representations of D_{3d} (Irrep). The seventh column gives the expansion of the accompanying form factors $h_{ab}(\mathbf{k})$ for small momentum, and the last column the associated physical process. The value of the coefficients for Bi₂Se₃ and other materials in this family can be found by first principles calculations (see for example Table IV in Ref. [17]).

Note that the three first terms in Table III are spin-independent: (0, 0) and (3, 0) are even and associated with intra-orbital hopping, while (2, 0) is odd and encodes inter-orbital hopping. The last three terms are spin-dependent and inter-orbital in character, therefore all odd. The terms (1, 1) and (1, 2) are associated with a Rashba-like spin-orbit coupling. The term (1, 3) is associated with trigonal warping of the Fermi surface and is usually dropped from the effective Hamiltonians since these carry at least terms of third order in momenta. Note that the coefficients C_1 , B_0 , and M_1 for CPSBS are smaller than the ones used for doped Bi₂Se₃ materials

given the presence of the PbSe layers. The Fermi surface of CPSBS was experimentally shown to be cylindrical (2D Fermi surface) [9], while the Fermi surface in doped Bi₂Se₃ materials can be either ellipsoidal (3D) or cylindrical (2D).

2. Classification of order parameters with momentum-independent gap matrices in the microscopic basis

Given these symmetries, we can classify all order parameters with \mathbf{k} -independent gap matrices in the microscopic basis according to the irreps of D_{3d} . Following [4], the order parameters can be generally written as:

$$\hat{\Delta} = \sum_{a,b} d_{ab} \hat{\tau}_a \otimes \hat{\sigma}_b (i\hat{\sigma}_2). \quad (\text{S3})$$

The allowed momentum-independent gap matrices can be determined by first searching for matrices satisfying $\hat{\Delta} = -\hat{\Delta}^T$, following fermionic antisymmetry. These can be classified according to the irreducible representations of D_{3d} , as displayed in Table IV. These order parameters are constructed in the orbital basis, so one needs to transform them to the band basis in order to discuss the presence of nodes and their locations. Following the discussion in the SM of [4], we find the nodes highlighted in the last two columns of Table IV.

[a,b]	Irrep	Spin	Orbital	Parity	Matrix Form	Zero at 3D FS	Zero at 2D FS
[0,0]	A_{1g}	Singlet	Intra	Even	$\hat{\tau}_0 \otimes \hat{\sigma}_0 (i\hat{\sigma}_2)$	-	-
[3,0]					$\hat{\tau}_3 \otimes \hat{\sigma}_0 (i\hat{\sigma}_2)$	-	-
[2,3]	A_{1u}	Triplet	Inter	Odd	$\hat{\tau}_2 \otimes \hat{\sigma}_3 (i\hat{\sigma}_2)$	-	-
[1,0]	A_{2u}	Singlet	Inter	Odd	$\hat{\tau}_1 \otimes \hat{\sigma}_0 (i\hat{\sigma}_2)$	along the k_z axis $k_x = k_y = 0$	-
[2,1]	E_u	Triplet	Inter	Odd	$\hat{\tau}_2 \otimes \hat{\sigma}_1 (i\hat{\sigma}_2)$	along the k_x axis $k_z = k_y = 0$	along the $k_x k_z$ plane* $k_y = 0$
[2,2]					$\hat{\tau}_2 \otimes \hat{\sigma}_2 (i\hat{\sigma}_2)$	along the k_y axis $k_z = k_x = 0$	along the $k_y k_z$ plane** $k_x = 0$

TABLE IV. Superconducting order parameters for materials in the family of Bi₂Se₃. Here we focus on the order parameters with momentum-independent gap matrices in the microscopic basis and highlight the associated irreducible representation (Irrep) and the spin, orbital character, and parity of the respective gap matrix. We write the order parameter in the matrix form $\hat{\tau}_a \otimes \hat{\sigma}_b (i\hat{\sigma}_2)$. Here we factor out $(i\hat{\sigma}_2)$ so that one can directly relate $b = 0$ to a singlet state and $b = \{1, 2, 3\}$ with the $\{x, y, z\}$ components of the d -vector parametrization for triplet states. * Nodes are lifted if trigonal warping is introduced in the (1,3) term in the normal state. ** Nodes are not lifted if trigonal warping is introduced in the (1,3) term in the normal state.

B. Symmetry reduction for the bulk of CPSBS

For CPSBS, the presence of the (PbSe)₅ layers reduces the point group symmetry to D_{1d} (isomorphic to C_{2h}). In CPSBS \hat{C}_3 is not a symmetry transformation anymore, but \hat{C}'_2 and $\hat{\sigma}_d$ are still valid symmetry operations which allow us to generate the character table for the reduced group from the table for D_{3d} . The point group D_{1d} is formed by four operations organized in four conjugacy classes, therefore there are four irreducible representations, as displayed in Table V. The irreducible representations from D_{3d} to D_{1d} are mapped as follows: $A_{1g/u} \rightarrow A_{1g/u}$, $A_{2g/u} \rightarrow A_{2g/u}$, $E_{g/u} \rightarrow \{A_{1g/u}, A_{2g/u}\}$. The last correspondence means that the two dimensional irreducible representations of D_{3d} are split in D_{1d} .

irrep	\hat{E}	\hat{C}'_2	\hat{P}	$\hat{\sigma}_d$
A_{1g}	+1	+1	+1	+1
A_{2g}	+1	-1	+1	-1
A_{1u}	+1	+1	-1	-1
A_{2u}	+1	-1	-1	+1

TABLE V. Character table for the point group D_{1d} obtained from a reduction of the character table for D_{3d} by eliminating the columns corresponding to the conjugacy classes labelled as $2\hat{C}_3$ and $2\hat{S}_6$.

1. Description of the normal state

Given the presence of parity and time-reversal symmetries, the only terms allowed in $\hat{H}_0(\mathbf{k})$ are the same as the ones enumerated for the case of D_{3d} symmetry, but now these are mapped to different irreducible representations. The main consequence for our model is that the parameter A_0 does not need to be the same for the (1,1) and (1,2) terms (see Table VI).

(a, b)	\hat{P}	\hat{C}'_2	$\hat{\sigma}_d$	Irrep	$h_{ab}(\mathbf{k})$
(0,0)	+1	+1	+1	A_{1g}	$C_0 + C_1 k_z^2 + C_2(k_x^2 + k_y^2)$
(2,0)	-1	-1	+1	A_{2u}	$B_0 k_z$
(3,0)	+1	+1	+1	A_{1g}	$M_0 + M_1 k_z^2 + M_2(k_x^2 + k_y^2)$
(1,1)	-1	-1	+1	A_{2u}	$-A_1 k_y$
(1,2)	-1	+1	-1	A_{1u}	$A_2 k_x$
(1,3)	-1	+1	-1	A_{1u}	$R_1 k_x(k_x^2 - 3k_y^2)$

TABLE VI. Parametrization of the normal-state Hamiltonian given in Eq. (S2) for materials in the family of Bi_2Se_3 with reduced D_{1d} symmetry, applicable to the bulk of CPSBS. Note the different coefficients for (1,1) and (1,2) terms.

2. Order parameter discussion

Concerning the order parameters, the reduction of the point group symmetry in principle allows for new kinds of superpositions, as suggested by Table I in the main text. Note that [0,0] and [3,0] belong to A_{1g} , [2,3] and [2,2] belong to A_{1u} , and that [1,0] and [2,1] belong to A_{2u} . According to experiments, the order parameter that is in agreement with the symmetry protected nodes in the bulk of CPSBS is [2,2]. By symmetry, the most general form of the order parameter in D_{1d} is a linear superposition of [2,2] and [2,3]. A superposition of these two types of order parameters generally lifts the nodes present in the case of a pure [2,2] order parameter. The mixing of [2,2] and [2,3] order parameters is only possible in the presence of both SOC terms (1,2) and (1,3) in the normal state Hamiltonian. As the trigonal warping term (1,3) is negligibly small, this mixing should also be small in the bulk. The smallness of trigonal warping explains the robustness of the nodes (or their transformation to near nodes with experimentally inaccessible minima) in the bulk of CPSBS.

C. Symmetry reduction at the surface of CPSBS

At the surface of CPSBS, inversion symmetry is broken and the group is reduced to C_{1v} with only two elements, therefore only two conjugacy classes and irreducible representations. The irreps are mapped according to $\{A_{1g}, A_{2u}\} \rightarrow A_1$ and $\{A_{2g}, A_{1u}\} \rightarrow A_2$, as indicated by the C_{1v} character table displayed as Table VII.

irrep	\hat{E}	$\hat{\sigma}_d$
A_1	+1	+1
A_2	+1	-1

TABLE VII. Character table for the point group C_{1v} obtained by reducing the character table for D_{1d} by eliminating the columns corresponding to \hat{P} and \hat{C}'_2 .

1. Description of the normal state

Note that in the absence of inversion symmetry all (a, b) terms in the normal state Hamiltonian are symmetry allowed. The new terms in the normal state Hamiltonian are summarized in Table VIII.

2. Order parameter discussion

The order parameters are now mapped such that [0,0], [3,0], [1,0], and [2,1] belong to the A_1 irrep, while [2,3] and [2,2] belong to the A_2 irrep. Note that the latter is the same type of mixing found for D_{1d} symmetry. Again, according to experiments, the order parameter that is in agreement with the symmetry protected nodes in CPSBS is [2,2]. By symmetry, the most general form of the order parameter in C_{1v} is a linear superposition

(a, b)	$\hat{\sigma}_d$	TRS	Irrep	$h_{ab}(\mathbf{k})$	Process
(0, 0)	+1	+	A_1	$C_0 + C_1 k_z^2 + C_2(k_x^2 + k_y^2)$	Intra-orbital hopping
(0, 1)	+1	-	A_1	$c_1 k_y + c'_1 k_z$	SOC
(0, 2)	-1	-	A_2	$c_2 k_x + c'_2 k_x(k_x^2 - 3k_y^2)$	SOC
(0, 3)	-1	-	A_2	$c_3 k_x + c'_3 k_x(k_x^2 - 3k_y^2)$	SOC
(1, 0)	+1	+	A_1	$c_4 + c'_4 k_z^2 + c''_4(k_x^2 + k_y^2)$	Inter-orbital hopping
(1, 1)	+1	-	A_1	$-A_1 k_y + a_1 k_z$	SOC
(1, 2)	-1	-	A_2	$A_2 k_x$	SOC
(1, 3)	-1	-	A_2	$R_1 k_x(k_x^2 - 3k_y^2) + r_1 k_x$	SOC
(2, 0)	+1	-	A_1	$B_0 k_z + b_0 k_y$	Inter-orbital hopping
(2, 1)	+1	+	A_1	$c_5 + c'_5 k_z^2 + c''_5(k_x^2 + k_y^2)$	SOC
(2, 2)	-1	+	A_2	$c_6 k_x k_z + c'_6 k_y k_z$	SOC
(2, 3)	-1	+	A_2	$c_7 k_x k_z + c'_7 k_y k_z$	SOC
(3, 0)	+1	+	A_1	$M_0 + M_1 k_z^2 + M_2(k_x^2 + k_y^2)$	Intra-orbital hopping
(3, 1)	+1	-	A_1	$c_8 k_y + c'_8 k_z$	SOC
(3, 2)	-1	-	A_2	$c_9 k_x + c'_9 k_x(k_x^2 - 3k_y^2)$	SOC
(3, 3)	-1	-	A_2	$c_{10} k_x + c'_{10} k_x(k_x^2 - 3k_y^2)$	SOC

TABLE VIII. Parametrization of the normal-state Hamiltonian given in Eq. (S2) for materials in the family of Bi_2Se_3 with reduced C_{1v} symmetry, applicable to the surface of CPSBS. Here we entered new symmetry allowed coefficients b_0 , a_1 , r_1 , and c_i , c'_i , and c''_i , for $i = \{1, \dots, 10\}$.

of $[2, 2]$ and $[2, 3]$. As discussed above, the mixing of these two types of order parameters would generally lift the nodes. Note that, in presence of only C_{1v} symmetry, these two order parameter components can be coupled by multiple pairs of terms in the normal state Hamiltonian.

D. Symmetry reduction at the surface of CPSBS with disorder

At the surface of CPSBS, superconductivity was only observed in areas with no stripe pattern. This suggests that the influence of the PbSe layers in the superconducting areas is weakened and the three-fold rotational symmetry of the Bi_2Se_3 layers in the bulk is restored in these regions. We consider then the point group symmetry of the surface of Bi_2Se_3 , identified as C_{3v} . The irreps are mapped according to $\{A_{1g}, A_{2u}\} \rightarrow A_1$, $\{A_{2g}, A_{1u}\} \rightarrow A_2$, and $\{E_u, E_g\} \rightarrow E$, as indicated by the C_{3v} character table displayed as Table IX.

irrep	\hat{E}	$2\hat{C}_3$	$3\hat{\sigma}_d$
A_1	+1	+1	+1
A_2	+1	+1	-1
E	2	-1	0

TABLE IX. Character table for the point group C_{3v} obtained by reducing the character table for D_{3d} by eliminating the columns corresponding to \hat{P} , $3\hat{C}'_2$, and $2\hat{S}_6$.

1. Description of the normal state

Note that in the absence of inversion symmetry all (a, b) terms in the normal state Hamiltonian are symmetry allowed. The new terms in the normal state Hamiltonian are summarized in Table X.

(a, b)	$\hat{\sigma}_d$	TRS	Irrep	$h_{ab}(\mathbf{k})$	Process
(0, 0)	+1	+	A_1	$C_0 + C_1 k_z^2 + C_2(k_x^2 + k_y^2)$	Intra-orbital hopping
(0, 1)	+1	-	E	$m_1 k_y$	SOC
(0, 2)	-1	-	E	$-m_1 k_x$	SOC
(0, 3)	-1	-	A_2	$m_2 k_x(k_x^2 - 3k_y^2)$	SOC
(1, 0)	+1	+	A_1	$m_3 + m'_3 k_z^2 + m''_3(k_x^2 + k_y^2)$	Inter-orbital hopping
(1, 1)	+1	-	E	$-A_0 k_y$	SOC
(1, 2)	-1	-	E	$A_0 k_x$	SOC
(1, 3)	-1	-	A_2	$R_1 k_x(k_x^2 - 3k_y^2)$	SOC
(2, 0)	+1	-	A_1	$B_0 k_z$	Inter-orbital hopping
(2, 1)	+1	+	E	$m_4(k_x^2 - k_y^2)$	SOC
(2, 2)	-1	+	E	$-m_4 k_x k_y$	SOC
(2, 3)	-1	+	A_2	$m_5 k_x k_z(3k_x^2 - k_y^2)$	SOC
(3, 0)	+1	+	A_1	$M_0 + M_1 k_z^2 + M_2(k_x^2 + k_y^2)$	Intra-orbital hopping
(3, 1)	+1	-	E	$m_6 k_y$	SOC
(3, 2)	-1	-	E	$-m_6 k_x$	SOC
(3, 3)	-1	-	A_2	$m_7 k_x(k_x^2 - 3k_y^2)$	SOC

TABLE X. Parametrization of the normal-state Hamiltonian given in Eq. (S2) for materials in the family of Bi_2Se_3 with reduced C_{3v} symmetry, applicable to the surface of doped Bi_2Se_3 and the disordered surfaces of CPSBS. Here we entered new symmetry allowed coefficients m_i , m'_i , and m''_i , for $i = \{1, \dots, 7\}$.

E. Parametrization of normal state Hamiltonian and gaps for Figure 5 in the main text

For the generation of Figure 5, we used the following first principle parameters extracted from Ref. [12] for the starting Hamiltonian with D_{3d} symmetry:

$$\begin{aligned}
A_0 &= 3.33 \text{ eV}\text{\AA}^{-1}, \\
C_0 &= -0.0083 \text{ eV}, \\
C_2 &= 30.4 \text{ eV}\text{\AA}^{-2}, \\
M_0 &= -0.28 \text{ eV}, \\
M_2 &= 44.5 \text{ eV}\text{\AA}^{-2}, \\
R_1 &= 50.6 \text{ eV}\text{\AA}^{-3}.
\end{aligned} \tag{S4}$$

We set $B_0 = C_1 = M_1 = 0$ (in the respective units) to eliminate the k_z dependence.

In the presence of D_{1d} symmetry, $A_1 \neq A_2$. As we do not have access to first principles calculations, we choose $A_{1,2} = A_0 \pm A_0/10$. The gap anisotropy does not seem to strongly depend on the ratio A_1/A_2 .

For the new terms at the surface, we also do not have access to a first principles calculation, so we set these to be a fixed percentage (p) of the value of terms with similar momentum dependence in the original normal state Hamiltonian with inversion symmetry.

For the case with D_{1d} symmetry we set

$$\begin{aligned}
c_1 &= b_0 = c_8 = -pA_1 \\
c_2 &= c_3 = c_9 = c_{10} = pA_2 \\
c'_2 &= c'_3 = c'_9 = c'_{10} pR_1 \\
c_4 &= c_5 = pC_0 \\
c'_4 &= c'_5 = pC_1, \\
c''_4 &= c''_5 = pC_2 \\
r_1 &= pA_2
\end{aligned} \tag{S5}$$

and take $a_1 = c_6 = c'_6 = c_7 = c'_7 = c'_8 = 0$ to eliminate the k_z dependence.

For the case with C_{3v} symmetry we set

$$\begin{aligned}
m_1 &= m_6 = pA_0 \\
m_2 &= m_7 = pR_1 \\
m_3 &= pC_0 \\
m'_3 &= pC_1 \\
m''_3 &= pC_2
\end{aligned} \tag{S6}$$

and take $m_4 = 0$ as there is no such terms in our parametrization of the normal state Hamiltonian with D_{3d} symmetry, and we take $m_5 = 0$ to eliminate the k_z dependence.

For Figure 5 in the main text, we used a chemical potential shift of $\mu = 0.4\text{eV}$, the order parameter magnitude of $d = 0.01\text{eV}$, and the surface factor $p = 0.01$. For the gap with C_{1v} symmetry we choose $d_{22}/d_{23} = \sqrt{2}$ and for the gap with C_{3v} symmetry we choose $d_{22}/d_{21} = 1$. The choice of p and ratio of order parameters were such that we could find order parameter superpositions that have gap anisotropy and gap minima rotation comparable to the experimental observations. A more microscopic derivation of such parameters would be desirable, but goes beyond the scope of this work.

-
- [1] Eskildsen, M. R. et al. Vortex imaging in the π band of Magnesium Diboride. *Phys. Rev. Lett.* **89**, 187003 (2002).
 - [2] Bergeal, N. et al. Scanning tunneling spectroscopy on the novel superconductor CaC_6 . *Phys. Rev. Lett.* **97**, 077003 (2006).
 - [3] Renner, C., Kent, A. D., Niedermann, P., Fischer, O. & Lévy, F. Scanning tunneling spectroscopy of a vortex core from the clean to the dirty limit. *Phys. Rev. Lett.* **67**, 1650–1652 (1991).
 - [4] Andersen, L., Ramires, A., Wang, Z., Lorenz, T. & Ando, Y. Generalized Anderson’s theorem for superconductors derived from topological insulators. *Sci. Adv.* **6**, eaay6502 (2020).
 - [5] Tao, R. et al. Direct visualization of the nematic superconductivity in $\text{Cu}_x\text{Bi}_2\text{Se}_3$. *Phys. Rev. X* **8**, 041024 (2018).
 - [6] Bagchi, M., Brede, J. & Ando, Y. Observability of superconductivity in Sr-doped Bi_2Se_3 at the surface using scanning tunneling microscope. *Phys. Rev. Mater.* **6**, 034201 (2022).
 - [7] Nagai, Y. Field-angle-dependent low-energy excitations around a vortex in the superconducting topological insulator $\text{Cu}_x\text{Bi}_2\text{Se}_3$. *J. Phys. Soc. Jpn.* **83**, 063705 (2014).
 - [8] Nakayama, K. et al. Manipulation of topological states and the bulk band gap using natural heterostructures of a topological insulator. *Phys. Rev. Lett.* **109**, 236804 (2012).
 - [9] Nakayama, K. et al. Observation of two-dimensional bulk electronic states in the superconducting topological insulator heterostructure $\text{Cu}_x(\text{PbSe})_5(\text{Bi}_2\text{Se}_3)_6$: Implications for unconventional superconductivity. *Phys. Rev. B* **92**, 100508 (2015).
 - [10] Andersen, L., Wang, Z., Lorenz, T. & Ando, Y. Nematic superconductivity in $\text{Cu}_{1.5}(\text{PbSe})_5(\text{Bi}_2\text{Se}_3)_6$. *Phys. Rev. B* **98**, 220512 (2018).
 - [11] Zhang, H. et al. Topological insulators in Bi_2Se_3 , Bi_2Te_3 and Sb_2Te_3 with a single Dirac cone on the surface. *Nature Physics* **5**, 438–442 (2009).
 - [12] Liu, C.-X. et al. Model Hamiltonian for topological insulators. *Phys. Rev. B* **82**, 45122 (2010).